

10/15/04

**Precipitation and Latent Heating Distributions
from Satellite Passive Microwave Radiometry
Part II: Evaluation of Estimates Using Independent Data**

Song Yang^a, Williams S. Olson^b, Jian-Jian Wang^c,
Thomas L. Bell^d, Eric A. Smith^d, Christian D. Kummerow^e

^aSchool of Computational Science, George Mason University, Fairfax, VA

^bJCET/University of Maryland Baltimore County, Baltimore, MD

^cGEST/University of Maryland Baltimore County, Baltimore, MD

^dGoddard Space Flight Center, Greenbelt, MD

^eColorado State University, Fort Collins, CO

To be submitted October 2004

Corresponding Author Address: Dr. Song Yang, NASA/GSFC, Code 912.1, Greenbelt, MD
20771. ysong@agnes.gsfc.nasa.gov

Abstract

Rainfall rate estimates from space-borne instruments are generally accepted as reliable by a majority of the atmospheric science community. One of the Tropical Rainfall Measuring Mission (TRMM) facility rain rate algorithms is based upon passive microwave observations from the TRMM Microwave Imager (TMI). Part I of this study describes improvements in the TMI algorithm that are required to introduce cloud latent heating and drying as additional algorithm products. Here, estimates of surface rain rate, convective proportion, and latent heating are evaluated using independent ground-based estimates and satellite products.

Instantaneous, 0.5° -resolution estimates of surface rain rate over ocean from the improved TMI algorithm are well correlated with independent radar estimates ($r \sim 0.88$ over the Tropics), but bias reduction is the most significant improvement over forerunning algorithms. The bias reduction is attributed to the greater breadth of cloud-resolving model simulations that support the improved algorithm, and the more consistent and specific convective/stratiform rain separation method utilized. The bias of monthly, 2.5° -resolution estimates is similarly reduced, with comparable correlations to radar estimates. Although the amount of independent latent heating data are limited, TMI estimated latent heating profiles compare favorably with instantaneous estimates based upon dual-Doppler radar observations, and time series of surface rain rate and heating profiles are generally consistent with those derived from rawinsonde analyses. Still, some biases in profile shape are evident, and these may be resolved with (a) additional contextual information brought to the estimation problem, and/or (b) physically-consistent and representative databases supporting the algorithm.

A model of the random error in instantaneous, 0.5° -resolution rain rate estimates appears to be consistent with the levels of error determined from TMI comparisons to collocated radar. Error model modifications for non-raining situations will be required, however. Sampling error appears to represent only a fraction of the total error in monthly, 2.5° -resolution TMI estimates; the remaining error is attributed to physical inconsistency or non-representativeness of cloud-resolving model simulated profiles supporting the algorithm.

1. Introduction

In Part I (Olson et al. 2004), an improved method for inferring precipitation and atmospheric latent heating profiles from satellite passive microwave radiometer measurements was described, and random errors due to algorithm and sampling deficiencies were estimated. This method represents the current (Version 6, or V6) Tropical Rainfall Measuring Mission (TRMM) facility algorithm applied to passive microwave observations from the TRMM Microwave Imager, or TMI. TRMM is the first joint satellite project between the United States and Japan dedicated to the measurement of tropical rainfall and latent heating distributions (Simpson et al., 1988). Previous TMI algorithms produced estimates of surface rain rates and vertical precipitation profiles but not latent heating profiles. The evolution and improvement of the official TRMM TMI algorithms through Version 5 (V5) are documented in Kummerow et al. (2001).

In addition to the TMI, the TRMM observatory includes the first spaceborne weather radar, or Precipitation Radar (PR). The TRMM standard precipitation algorithm for applications to the PR was developed by Iguchi et al. (2000). Since the PR provides much higher resolution depictions of both vertical and horizontal precipitation structures than the TMI, this alternative algorithm should in principle provide more accurate estimates of precipitation. However, contamination of the PR observations by surface backscatter at off-nadir viewing angles restricts the PR's useful swath width to approximately 215 km for a nominal TRMM satellite altitude of 350 km. By contrast, the TMI and most current satellite microwave imagers are conically scanning, which allows for uniform-resolution observations over swaths of several hundreds of kilometers width for nominal satellite altitudes. Because of their limited swath width and additional weight and power consumption, spaceborne radars assume the role of "calibrators" of passive microwave precipitation estimates, while the passive radiometers, already a component of several polar-orbiting observatories, provide more extensive sampling of precipitation events over the globe.

In addition, passive microwave estimates of precipitation and latent heating can be evaluated using independent estimates derived from ground-based radars (including single- and dual-Doppler configurations) and rawinsonde observation networks. As part of TRMM, radar data are collected continuously at four ground validation sites in the Tropics. These data have

been supplemented by dual-Doppler radar and rawinsonde observations from field campaigns in the South China Sea, western Brazil, and the vicinity of Kwajalein Atoll.

In the present study, V6 and V5 TMI estimated rain rates and latent heating profiles are compared to coincident estimates from both ground-based systems and PR-based algorithms as a test of consistency. It is not possible to “validate” the TMI estimates in a strict sense, since validation requires comparison to independent measurements that have much less uncertainty than the TMI estimates, and this is not always the case. On the other hand, the independent measurements do provide a useful reference and help identify possible biases and general levels of uncertainty associated with the TMI estimates. Also, the independent data are used to illustrate the changes in rain rate estimates derived from the current V6 TMI method relative to the previous technique from which it is descended (V5). Since latent heating was not a standard product of the V5 satellite algorithm or any previous version, current latent heating estimates are not compared to any previous estimates.

In section 2, the various data sources and products utilized in this study are described in detail. TMI surface rain rate estimates are compared to surface radar and PR estimates at different time and space resolutions in Section 3. Section 4 is devoted to comparisons of V6 TMI rain rate and latent heating profile estimates to independent estimates from ground-based systems, and a summary and discussion are provided in Section 5.

2. Datasets

The focus of the current study is on the estimation of three parameters from satellite data: the surface rainfall rate, the convective proportion of rain, and the vertical profile of latent heating, defined here as the apparent heat source (total heating) less the radiative heating rate, or $Q_1 - Q_R$; see Yanai et al. 1973. The quantity $Q_1 - Q_R$ thus emphasizes the heating due to phase changes of water substance in precipitating clouds. The surface rainfall rate and the convective proportion of rain are standard outputs of both the V5 and V6 TMI algorithms. The V5 TMI algorithm is described in Kummerow et al. (2001), while the modifications that resulted in V6 are described in Part I (Olson et al. 2004) of the current study. Attempts to derive the latent heating profile based upon the V5 algorithm led to vertical heating structures that were not consistent with long-term climatologies based upon rawinsonde budget analyses (Tao et al.

2001). As explained in Part I, key improvements in the classification of convective and stratiform precipitation regions and the constraint on total rain area within the TMI footprint are expected to result in more realistic latent heating estimates from the V6 algorithm. Therefore, the vertical latent heating profile is provided as standard output from the V6 algorithm.

The sampling resolution of the TMI is about 14 km along-track and 5 km cross-track, and the spatial resolution of each measurement varies with channel frequency from about 48 km at 10.7 GHz to 6 km at 85.5 GHz. The V6 TMI precipitation products are designed to have an intermediate spatial resolution of 14 km x 14 km (see Part I), while V5 products have comparable resolution.

In order to demonstrate the performance of the TMI algorithm, precipitation products from V5 and V6 are compared to independent rain estimates at different time and space scales. The traditional "ground truth" for surface rain rates is derived from ground-validation (GV) radar, a key element in the algorithm evaluation process. There are four TRMM GV field sites serviced by the TRMM validation project; however, the Kwajalein Atoll site was specifically designed to provide data characteristic of a tropical oceanic environment. A map of the Kwajalein field site is shown in Fig. 1. Standard Version 3 TRMM GV output products are derived from each radar volume out to a range of 150 km; surface rain rate and convective/stratiform classification are interpolated to a 2 km x 2 km resolution horizontal grid. The radar sampling interval is 10 minutes, and so the radar map closest to the TRMM satellite overpass time is utilized for intercomparisons. In the current study, all significant rain events observed coincidentally by the TMI and the Kwajalein radar during 1998 are collected, yielding the 22 events depicted in Fig. 2. The event on March 25 did not produce any rain inside the TRMM swath, and so it is not included in the comparisons. The Kwajalein GV radar rain rates are adjusted using coincident raingage measurements to remove the radar-raingage bias over monthly periods; see Wolff et al. (2004). Due to the limited number of functioning raingages in particular months, however, the bulk adjustment of GV radar Z-R relations (convective and stratiform) was based upon coincident radar and raingage data from multiple months. Over 1998 as a whole, the (unadjusted) radar to raingage ratio based upon all coincident radar-raingage pairs was 1.24 with a correlation of 0.98.

Since the TRMM GV sites yield rain rate and convective proportion information at only a limited number of locations in the Tropics, products derived from the spaceborne PR are also

considered in the current investigation. Surface rain rate at each PR footprint location is a standard TRMM product derived using the algorithm of Iguchi et al. (2000). The classification of each PR footprint as convective/stratiform/undetermined is also a standard product, based upon the method of Awaka et al. (1998). Version 5 of these products is used for intercomparisons. The scan geometry and sampling rate of the PR lead to footprints spaced approximately 4.3 km cross- and down-track, over a 215 km wide swath centered within the 760 km wide TMI swath; therefore, TMI and PR observations over the PR swath are nearly coincident in space and time, aside from the 57 s offset in observation time caused by the difference in scan geometries of the sensors. The PR measurements themselves have an intrinsic spatial resolution of about 4.3 km, due to the diffraction limitation of the instrument. In a comparison of PR near-surface rain rates and collocated WSR-88D radar at Melbourne, Florida (one of the TRMM ground validation radars), Liao et al. (2001) noted a high bias of 3% and a standard error of 44% in PR rain estimates on an overpass-by-overpass basis, with a correlation between PR and ground validation rain estimates of 0.95. The relatively large standard error percentage results from the large population of light rains that contribute to the mean rain rate, and so this statistic does not necessarily reflect the good consistency between PR and ground radar. Schumacher and Houze (2000) also noted good agreement between PR and ground validation radar estimates of rain rates at Kwajalein. They reported biases of 6% or less, depending on the Z-R relations applied to the radar data, and a PR-ground validation radar rain rate correlation of 0.96. In both the Melbourne and Kwajalein radar comparisons, the mean convective and stratiform rain rates from PR agreed with the ground radar amounts to within 21%.

Following the discussion of estimated TMI product uncertainties in Part I, intercomparisons of TMI precipitation products and independent estimates are carried out at time and space resolutions that reflect potential applications of the products. Assimilation of surface rain rate or latent heating profiles into global climate or numerical weather prediction model analyses/forecasts requires instantaneous products at half-degree (or comparable) spatial resolution; see Krishnamurti et al. (2001); Hou et al. (2004). Consequently, instantaneous rainfall rates and convective proportion estimates at 0.5° resolution are compared in this study. Since the spatial sampling of TMI, GV radar, and PR are all relatively fine over $0.5^\circ \times 0.5^\circ$

latitude/longitude grid boxes, instantaneous precipitation estimates from each of the three sensors are simply averaged to obtain half-degree products for the intercomparisons.

Alternatively, climate or large-scale analysis studies may only require lower-resolution estimates. When TMI precipitation estimates are averaged over the period of one month in $2.5^\circ \times 2.5^\circ$ latitude/longitude grid boxes, the random error due to the limited information content of the radiometer data becomes fairly negligible, although sampling error can be significant; see Part I. As observations from a greater number of spaceborne microwave radiometers in the Global Precipitation Measurement (GPM) mission "constellation" become available, sampling error will also be greatly reduced in monthly estimates, revealing the space and time variations that hopefully will define trends in large-scale precipitation and latent heating. Therefore, as a test of a proxy climate product, monthly-mean 2.5° TMI estimates are compared to independent estimates from the PR. These products are created by averaging all instantaneous precipitation estimates falling in a particular $2.5^\circ \times 2.5^\circ$ latitude/longitude box in a specified month.

At either instantaneous 0.5° or monthly 2.5° resolution, precipitation products are not included in statistics if both the TMI and the independent product are non-raining pairs. Since, at a given location, rain typically occurs less than about 10% of the time, eliminating non-raining pairs in the statistics emphasizes the algorithm's ability to quantify precipitation where it is raining. When instantaneous imagery is compared, either GV radar or PR estimates are averaged within a 196 km^2 ($14 \text{ km} \times 14 \text{ km}$) circular area centered on a given TMI observation to approximate the resolution of the TMI instantaneous, footprint-scale estimates.

Since there are no direct latent heating measurements, two alternative approaches are used to evaluate TMI latent heating rate estimates. The first method is founded on the assumption that the dominant contribution to diabatic heating comes from the vertical advection of dry static energy; e.g. Cifelli and Rutledge (1998). In this approximation,

$$w \frac{\partial s}{\partial z} = Q_1, \quad (1)$$

where w is the vertical velocity, s is the dry static energy ($c_p T + gz$), and z is altitude. Here, c_p is the specific heat of air at constant pressure, T is temperature, and g is the acceleration of gravity. The vertical velocity can be calculated using dual-Doppler radar observations: Dual-Doppler analysis yields the horizontal wind speed and direction; by vertically integrating the divergence of the horizontal wind, one obtains the vertical velocity subject to a prescribed vertical velocity

at the top or bottom of the air column; see Doviak et al. (1976), Davies-Jones (1979). The dry static energy is calculated from sounding data coinciding with the dual-Doppler observations. Combining the dual-Doppler vertical velocities and dry static energy gradient in (1) yields a “dual-Doppler study” (DDS) estimate of latent heating.

During the TRMM field campaign at Kwajalein (KWAJEX; 23 July – 15 September, 1999), an S-band radar on the Kwajalein Atoll and a C-band radar aboard the Research Vessel Ron H. Brown provided dual-Doppler coverage of precipitation systems over the Pacific Ocean. The RV Ron Brown was positioned 40 km south of the Kwajalein Atoll radar site, and this configuration allowed for dual-Doppler coverage within the two 80 km-diameter circular “lobes” for which the crossing angle of radar rays was greater than 30° ; see Fig. 1. Unfortunately, there were relatively few dual-Doppler radar observations of KWAJEX rain events that coincided with TRMM satellite overpasses. From KWAJEX, only five such events have been identified, and only two involve organized mesoscale convective systems. In spite of the difficulties in calculating vertical velocity from dual-Doppler observations and the relatively few storms observed during TRMM overpasses, observations of the two organized systems are analyzed here, and the resulting latent heating profiles are compared to estimates from the V6 TMI algorithm. The primary advantage of the dual-Doppler estimates of latent heating is that they provide an “instantaneous” sample of the heating distribution at relatively high spatial resolution. The main source of error in the calculation of the heating rate using (1) is the error in the derivation of the vertical velocity. Although the measurement of the horizontal winds and horizontal divergence from the dual-Doppler analysis is fairly accurate, vertical velocities are calculated from mass continuity by integrating the horizontal divergence vertically. In the current study, a variational adjustment scheme is utilized to constrain the divergence integral subject to boundary conditions on the vertical velocity at the surface and cloud top; see O’Brien (1970). Nevertheless, errors in dual-Doppler estimates of vertical velocity are generally within 10%, but could be up to 30% in extreme cases, based upon an earlier study involving coincident sailplane observations (see Doviak and Zmic, 1993). Percentage errors of comparable magnitudes are expected in estimates of Q_I using (1). As a result, error envelopes up to 30% are shown in the DDS estimates of Q_I in the current study.

Even though spatial averaging of passive microwave precipitation and latent heating estimates is required to control the random error of the estimates (Olson et al. 1999, Shige et al.

2004), the fact that DDS heating estimates can be matched in time with satellite estimates is an advantage with respect to rawinsonde-based estimates of latent heating, which have relatively low temporal and spatial resolution. The rawinsonde-based estimates of latent heating utilized in this study are now described.

Yang and Smith (1999a, 2000) utilized rawinsonde-derived apparent heat source (Q_1) and apparent moisture sink (Q_2) budget estimates from the Tropical Ocean Global Atmosphere Coupled Ocean-Atmosphere Response Experiment (TOGA COARE) network to validate their latent heating estimates from SSM/I data. Results indicated the credibility of latent heating estimates derived from SSM/I data, although there were some uncertainties at the daily time-scale. SSM/I latent heating estimates from a different algorithm were compared to a TOGA COARE time series of Q_1 by Olson et al. (1999), with similar results. More recently, Tao et al. (2001) demonstrated that several satellite-based estimates of space-time mean latent heating profiles were compatible with the mean rawinsonde-derived heating profiles from the TOGA COARE field campaign's Intensive Flux Array over the Nov. 1992 - Feb. 1993 intensive observing period. These studies provided evidence that rawinsonde analyses could be used to evaluate satellite latent heating estimates; however, since rawinsonde networks covering oceanic areas have relatively limited time and space sampling (2-4 launches day⁻¹, and ~1 site per 10⁴ km²), rawinsonde analyses are best suited for relatively large time/space-scale comparisons.

In the present study, analyses of Q_1 from the Northern Enhanced Sounding Array (NESA) of the South China Sea Monsoon Experiment (SCSMEX) are compared to estimates of Q_1 - Q_R from the V6 TMI algorithm. The rawinsonde sites associated with the NESA, located in the northern portion of the South China Sea, are depicted in Fig. 3. The rawinsonde-based estimates of Q_1 are derived from the analyses of Johnson and Ciesielski (2002) for the period 15 May - 20 June 1998 over the NESA. During the specified period, rawinsondes were launched 2-4 day⁻¹ at stations along the perimeter of the NESA and 4 day⁻¹ from Dongsha Island and the Research Vessel Shiyan #3, located near the center of the array. Outside the array, rawinsondes were typically launched 3-4 day⁻¹. The rawinsonde data were interpolated to a 1° resolution grid, with large data gaps filled in using GEWEX Asian Monsoon Experiment (GAME) Reanalysis values; see Yamazaki et al. (2000) for a description of the GAME Reanalysis. Vertical motion was derived by integrating the horizontal divergence upward from the surface, with the divergence adjusted to achieve mass balancing. The analyzed temperatures, specific humidities,

and winds were used to estimate mean Q_1 and Q_2 profiles within the NESAs at 00, 06, 12, and 18 UTC during the specified period.

In addition to Q_1 and Q_2 , estimates of the surface rain rate over the NESAs by Johnson and Ciesielski (2002) were derived from the moisture budget,

$$\langle Q_2 \rangle = L_v (P - E), \quad (2)$$

where $\langle Q_2 \rangle$ is the vertical integral of Q_2 , L_v is the latent heat of vaporization, P is the surface precipitation rate, and E is the surface evaporation rate. Surface evaporation over the NESAs was obtained from the GAME Reanalysis values, adjusted by shipboard flux measurements from the Shiyang #3; see Johnson and Ciesielski (2002) for a description of the procedure. Given $\langle Q_2 \rangle$ and E , the surface precipitation rate is derived from (2).

In order to reduce errors due to the relatively coarse temporal sampling of the NESAs by the TMI (about 1.4 day⁻¹) and rawinsondes, a 3-day running mean filter is applied to the domain-average estimated heating profiles and surface rain rates within the NESAs from both the TMI and the rawinsonde analyses. Mean heating profiles and rain rates are also calculated for the entire 15 May – 20 June 1998 period. Sampling errors in rawinsonde-based analyses for several sounding arrays were estimated by Mapes et al. (2003). Errors in NESAs surface rainfall rates from the Q_2 budget are reduced to 1.3 mm day⁻¹, or about 30% of the long-term mean rain rate, using 3-day averages. Similar averaging reduces the error in the altitude of the peak Q_1 to 47 hPa, or about 800 m (at 7 km altitude), while a 30-day average will result in an error of 15 hPa or about 250 m (at 7 km altitude) in the altitude of the peak Q_1 .

3. Surface Rain Rate Intercomparisons

a. Footprint resolution

Prior to the evaluation of lower-resolution products, instantaneous maps of surface rain rate from V6 and V5 TMI, as well as collocated rain estimates from Kwajalein GV radar and PR, are compared to illustrate changes in the TMI algorithm. Horizontal distributions of retrieved rain rates from V6 TMI are generally consistent with those from V5 for each event we identified. This result was expected because V5 TMI rain rates had already exhibited reasonable agreement with GV radar (Kummerow et al. 2001). However, V6 rain estimates are greatly improved with

respect to V5 in coastal areas, since a new, higher-resolution geographical database is used to identify coastal boundaries in V6, and some footprints previously classified as coastal in V5 are now correctly identified as oceanic; see Part I. Using either the V5 or V6 algorithm, the TMI yields more ambiguous rain estimates for footprints classified as coastal, in contrast to ocean or land footprints, due to uncertainties in the microwave surface emissivity of coastal regions. All TMI footprints in the vicinity of the Kwajalein site in V6 are classified as oceanic because of the extremely small land area of Kwajalein and neighboring atolls.

The intercomparison cases shown in Fig. 4 are presented as examples of the improvements made to the V6 TMI algorithm. The images in the left panels correspond to the TRMM overpass at 17 UTC on 24 August 1998. Although the TMI observed the precipitation system near the Kwajalein GV site during this overpass, the system was outside the boundaries of the PR swath. Thus, only the GV rain map shown in the middle left panel is compared to the V6 and V5 TMI estimates. Note that in the proximity of Kwajalein and the Namu Atoll to the southeast, the V5 algorithm yields very little precipitation over ocean regions, while the V6 algorithm and the GV radar identify intense rains up to 20 mm h^{-1} . This discrepancy is exclusively due to the classification of ocean areas close to Kwajalein/Namu as "coastal" (mixed ocean-land) in the V5 algorithm, whereas the same regions are classified as "ocean" in the V6 algorithm. Only rain rates in regions classified as "ocean" are plotted in Fig. 4. Since all footprints in the vicinity of Kwajalein are classified as oceanic by the V6 algorithm (even those footprints over the atolls themselves, due to their very small land areas), rain intensity is quantified by both microwave emission from liquid precipitation as well as scattering. Rain intensity interpreted from microwave emission/scattering by the V6 algorithm results in rain estimates generally consistent with the GV estimates. If the same regions had been classified as "coastal", then a much less reliable scattering-only algorithm would have been applied to the TMI data as part of V6.

The right panels are based upon observations coinciding with the TRMM overpass at 17 UTC on 28 October 1998. In this case most of the precipitation fell beyond the range of the Kwajalein GV radar, and so PR rain estimates, shown in the middle panel, are compared to V6 (V5) TMI rain estimates in the top (bottom) panel. Since the TRMM PR has relatively high spatial resolution and better ability to detect light rains, the gradients of light rain along the edges of the rain system in the right-middle panel are considered accurate. (Note that the minimum

detectable surface rain rate from PR is roughly 0.3 mm h^{-1} , corresponding to a minimum detectable signal of 18 dBZ). The pattern of rainfall derived from V6 is generally more consistent with the PR estimate, while the V5 rain pattern exhibits none of the gradients along the precipitation boundaries seen in the PR imagery. The improved rain patterns of the V6 estimates are attributed to the expanded cloud-radiative model database supporting V6; the expanded database includes a better representation of isolated convection and weak precipitation events relative to the V5 supporting database; see Part I.

Since different ocean/land/coast classifications are used in the V5 and V6 TMI algorithms, in all of the plots and statistical analyses to follow only latitude/longitude grid boxes with essentially complete coverage (90% of the grid box area) by TMI, GV radar, and PR, with all footprints classified as ocean by the V5 TMI algorithm, are considered. The V5 classification is used because the focus of this study is changes in the ocean precipitation/latent heating estimation method, and the V5 ocean footprints are a subset of the V6 ocean footprints. Also, data pairs for which both sensors yield zero rain rates are excluded from the analysis in order to emphasize the skill of the algorithms in raining regions.

b. Instantaneous, $0.5^\circ \times 0.5^\circ$ estimates

Displayed in Figure 5 are scatterplots of oceanic instantaneous, $0.5^\circ \times 0.5^\circ$ mean surface rain rates at the Kwajalein site from V6 and V5 TMI versus Kwajalein GV radar and PR estimates, drawn from the 21 selected rain events during 1998. Statistics of these intercomparisons are provided in Table 1. It may be noted from the plots in Fig. 5a that rain rate estimates from both V6 and V5 TMI show reasonable agreement with the GV radar and PR near Kwajalein, although differences between the rain estimates are still evident. The correlations between the TMI estimates and either GV or PR improve slightly in the progression from V5 to V6, and V6 estimates are less biased and have lower random error. Convective rain rate estimates (Fig. 5b) are less correlated with GV or PR than total rain rate estimates, due to the less direct inference of convective or stratiform rain type from the passive microwave data. It is expected that the GV radar or PR can provide a more detailed picture of precipitation structure than TMI, although fundamental differences in the definitions of convective and stratiform rain types from GV, PR, and TMI can also lead to differences in estimated convective/stratiform rain proportion.

Although the evaluation of TRMM products near the ground validation sites has the advantage of the availability of raingage-calibrated ground radar observations (Wolff et al. 2004), the errors statistics represent only local conditions over the period of study. Because of the large spatio-temporal variations of precipitation, more general conclusions can be made from global comparative datasets. Therefore, all V6 and V5 instantaneous TMI precipitation estimates from July 2000 over ocean areas are compared to coincident PR estimates at $0.5^\circ \times 0.5^\circ$ resolution. Presented in Fig. 6a are scatterplots of the collocated TMI and PR estimates; V6 and V5 TMI estimates are plotted in the left and right columns, respectively. Statistics of the comparisons are given in Table 2. Again, both the V6 and V5 estimates of surface rain rate are well correlated with PR estimates; however, the V6 estimates have less bias and lower random error in relation to the V5 estimates.

Estimates of the convective rain rate are less correlated with PR and the bias and random error of these estimates is greater than the corresponding statistics of total rain. The less direct inference of convective precipitation structure from the TMI is the primary reason for the greater scatter of TMI convective rain rates relative to PR. Note that the V6 convective rain estimates are more high-biased with respect to the PR than the V5 estimates. The greater mean departure of V6 convective rain estimates is mainly attributed to the revised classification of convective/stratiform rain areas in the V6 algorithm; see Part I. The impact of the new classification is removed by considering a separation of the rain data based upon the PR classification of convective/stratiform rain areas. In Fig. 6b, the rain data are reclassified as "primarily convective", for which the PR convective rain proportion over each half-degree box is greater than 50% of the total PR rain, and "primarily stratiform", for which the PR convective proportion is less than 50%. Although there is not an obvious difference between the scatterplots of V6 and V5 "primarily convective" data, a significant decrease in the average intensity of V6 stratiform rains relative to V5 is evident.

The change in stratiform rainfall intensity is due to the revision of the method for determining convective and stratiform rain proportions in the TMI algorithm. In V5, the area fraction of convective precipitation within the nominal sensor footprint was used to constrain the selection of simulated precipitation profiles in the algorithm's supporting database; see Kummerow et al. (2001). In addition, the proximity of a footprint to convection was also used as a constraint; therefore, even footprints with no convective coverage might be assigned quasi-

convective precipitation structure if they were adjacent to footprints classified as convective. This “blurring” of the convective/stratiform characterization led to overestimates of rain intensity in stratiform regions. In V6, in addition to the convective area constraint, a constraint on the total rain area is imposed; see Part I. As a result, a better (if not specific) indicator of the relative proportions of convective and stratiform rain flux is supplied to the algorithm. Also, the constraint on the proximity to convection is removed to produce a more distinct separation of convective and stratiform rain regions in a given mesoscale convective system. This more distinct separation leads to lower-intensity stratiform rains and a lower overall bias of stratiform and total rain from the V6 algorithm, as indicated in Fig. 6. The discrepancy between the basic definitions of convective/stratiform rain areas in the V6 and PR algorithms will be the focus of a future study.

Overlaid on the V6 scatterplot of Fig. 6a is a fit to the mean algorithm-derived estimate of error standard deviation as a function of rain rate; see Part I.

$$\sigma_{\bar{R}} \equiv 0.930 \ln(\bar{R} + 1 \text{ mm h}^{-1}) \quad (3)$$

Here, $\sigma_{\bar{R}}$ and \bar{R} have units of mm h^{-1} . The expression (3) represents only that portion of the algorithm random error due to the limited information content of the radiometer data. It is apparent that the assumption of zero rain rate error in footprints classified as non-raining is a deficiency of the model, since significant errors are seen near the origin of the scatterplot. The relative contributions of errors to due uncertainties in PR estimates, spatial sampling mismatches, and errors in cloud-radiative modeling have yet to be determined, but the mean algorithm estimate of error given by (3), modified by errors in non-raining footprints, may be useful for data assimilation applications. A more specific estimate of the error in each half-degree rain estimate is given by the full model [Eq. (19) in Part I], but this requires an aggregation of the errors at footprint-scale.

Variations of precipitation system structure and frequency of occurrence over the globe should lead to inhomogeneous distributions of error in rain rate estimates from spaceborne sensors, due to the limited information these sensors provide with regard to the physical characteristics of observed precipitation systems. Berg and Kummerow (2002) examined the systematic differences in satellite-based rain rate estimates in the East and West Pacific and linked these to differences in precipitation structure. Yang and Smith (2004) demonstrated that the degree of consistency between different TRMM rain products varies time and space. Here,

V6 and V5 TMI rain rate estimates over the tropical oceans from July 2000 are broken down by region to uncover possible variations in error statistics.

Presented in Fig. 7 are scatterplots of TMI and PR rain rate estimates at 0.5° resolution; V6 TMI estimates are plotted in the left-hand column, while V5 TMI estimates are plotted in the right-hand column. Plotted in each V6-V5 pair of panels in a given row are data from one of five selected tropical $10^\circ \times 10^\circ$ areas, including areas in the West Pacific (WP), East Pacific (EP), Atlantic Ocean (AO), Indian Ocean (IO), and South China Sea (SCS). The boundaries of these areas are given in Table 3. Statistics of the regional comparisons are presented in Fig. 8.

It may be noted from the figures that the typical high biases of the V5 TMI estimates are generally reduced in the V6 estimates, and random errors decrease. This result holds independent of the specified region, even though the correlations of the estimates with collocated PR rain rates are nearly unchanged. The implication of these regional tests is that the modifications of the TMI algorithm in the progression from V5 to V6 corrected basic deficiencies that previously affected algorithm performance throughout the Tropics; however, based upon the limited samples of regional data utilized here, no general conclusions can be made.

c. Monthly, $2.5^\circ \times 2.5^\circ$ estimates

Intercomparisons of monthly-mean, 2.5° resolution V6 and V5 TMI and PR rain rate estimates over ocean from July 2000 are presented in Figure 9. Typically, greater averaging of passive microwave rain estimates has the effect of reducing the random retrieval error relative to the variance of the rain data, resulting in higher correlations of rain estimates with respect to independent data. Here, however, the correlations of both V6 and V5 rain estimates with respect to the PR are slightly less than the correlations of the instantaneous, 0.5° averages with respect to PR, shown previously; see Table 2. The likely explanation for the weaker correlations is that the suppression of random retrieval errors (due to the limited information content of the radiometer data) by averaging is offset by regionally-dependent systematic errors in algorithm estimates. The regionally-dependent systematic errors are relatively small, and only emerge in space-time averages over relatively large areas and long periods. These errors could include errors in the supporting cloud-radiative model simulations of the TMI supporting database or unrepresentative proportions of various precipitation system types in the database. Errors in the PR rain estimates

could also contribute to the overall scatter, however. Although the correlations of the monthly, 2.5° V6 and V5 estimates to PR estimates are the same, V6 estimates exhibit less bias with respect to PR.

Since the samples plotted in Fig. 9 are derived from only those time-coincident observations for which both TMI and PR observed most of a given 2.5 degree grid box, the primary contribution to differences in the monthly mean rain rates comes from differences in estimated rain intensities rather than differences in sampling. However, to provide some perspective on the relative magnitudes of rain estimation error and sampling error, an estimate of the mean TMI temporal sampling error is overlaid on the V6 plot. Following Bell and Kundu (2000), the percentage sampling error given by (23) of Part I is represented as a function of the monthly-mean rain rate at 2.5° resolution using the power-law fit,

$$\frac{\sigma_{\langle R \rangle}}{\langle R \rangle} \times 100\% \cong 20.5 \langle R \rangle^{-0.130}. \quad (4)$$

From Fig. 9 it may be noted that qualitatively, the mean TMI sampling error is only a fraction of the combined TMI and PR rain estimation error.

4. Latent Heating Comparison Results

a. Comparisons to dual-Doppler study estimates

The evaluation of latent heating estimates from satellite observations is always a difficult challenge, since there exist no independent, direct estimates of latent heating. Yang and Smith (1999b) approached this problem by analyzing the evolution of 3-D latent heating structures from SSM/I observations for well-known circulations associated with the El Niño and the Asian Monsoon to qualitatively determine the reliability of their latent heating estimates. Olson et al. (1999) compared time series of SSM/I-based estimates of latent heating to rawinsonde-based analyses of Q_1 over the Intensive Flux Array of TOGA COARE. The only intercomparison of latent heating profiles based upon TRMM sensor observations indicated that there was rough agreement in the horizontal and vertical distributions of heating derived from different participating algorithms (Tao et al. 2001); however, some discrepancies in the heating distributions were evident. Without careful comparisons to independent heating estimates at similar time and space scales, it is hard to ascertain the relative accuracy of the various algorithms.

As noted in section 2, heating estimated from the DDS method is only an approximation to the total diabatic heating; however, in convectively active regions the vertical structure of the heating from the DDS analysis should be similar to that of $Q_1 - Q_R$. Unfortunately, there are very few DDS cases from the KWAJEX field campaign that can be used for heating intercomparison studies. Figure 10 illustrates comparisons of the vertical heating structures from V6 TMI and DDS for two selected cases from the Kwajalein site. Shown in Fig 10a are fields coinciding with the TMI overpass at approximately 10 UTC on 15 August 1999, while the fields shown in Fig. 10b correspond to the overpass at 19 UTC on 29 July 1999.

The precipitation shown in the dual-Doppler radar lobes in Fig. 10a was produced by an organized mesoscale convective system that began as a westward-propagating convective line. The retrieved mean heating profile from TMI shows deep positive heating from 1 to 17 km, with a maximum near 6 km. Evaporative cooling is seen near the surface. Heating estimates from the DDS are limited in altitude by the height of the radar-detectable echo, but generally the more intense and extensive the rain system is, the deeper the DDS heating analysis. In this case, the mean DDS heating is limited to altitudes below 15 km. The DDS mean heating profile exhibits positive heating from the surface to 15 km, with a maximum near 7 km. The maximum DDS heating magnitude is greater than that derived from the TMI. Although the vertical distributions of heating from TMI and DDS are consistent from the surface to the level of maximum heating, the TMI heating in the upper troposphere generally exceeds the DDS heating.

The disturbance that produced the rain pattern shown in Fig. 10b was imbedded in an extensive east-west oriented band of precipitation that approached Kwajalein from the south. The overall depth of the precipitation from this system was less than that of the preceding case, resulting in a shallower, less intense heating maximum derived from TMI. Similar to TMI, significant heating from the DDS is confined to altitudes less than 10 km, although the peak DDS heating is greater than that of the TMI heating profile. The DDS heating maximum is sharper than the TMI maximum, but both analyses reveal maximum heating centered at 5-6 km altitude. As in the preceding case, the TMI algorithm yields weak heating in the upper troposphere that is not reflected in the DDS analysis.

There could be several reasons for the discrepancies between the mean TMI and DDS heating profiles. First, in applications to relatively intense precipitation systems, the TMI algorithm tends to bias heating estimates towards the mean of heating profiles stored in the

algorithm's supporting database, and this could explain the broad, but relatively weak, heating profiles produced by the algorithm; see Part I, section 4. On the other hand, there is relatively large uncertainty in estimating the vertical velocity from the DDS method. It may be noted from Fig. 10 that the magnitudes of heating profiles from TMI are generally located within the 30% error envelopes of the DDS heating profiles. High biases of the TMI profiles outside the DDS error envelopes occur in the upper troposphere, however.

In spite of the noted discrepancies, these comparisons at the Kwajalein site illustrate the V6 TMI algorithm's potential, at least in the lower to mid-troposphere, for capturing variations of latent heating vertical structure.

b. Comparisons to rawinsonde-based estimates

Although comparisons of instantaneous latent heating estimates from TMI and DDS analyses are optimal from a sampling perspective, the limited number of collocated observations makes it impossible to draw any general conclusions. The SCSMEX NESA rawinsonde analyses described in section 2 are based upon limited temporal sampling (up to 4 day^{-1}), but they provide a continuous record of the evolution of diabatic heating over the SCSMEX intensive observing period. Here, 3-day running mean estimates of rawinsonde Q_1 and surface rain rate (from the Q_2 budget; see section 2) are compared to similarly averaged TMI estimates ($\sim 1.4 \text{ day}^{-1}$ sampling) for the period beginning with the monsoon onset in the South China Sea on 15 May, through 20 June 1998.

The surface rain rate time series from TMI and the rawinsonde analyses are shown in the top panel of Fig. 11. This comparison is a good indicator of the relative sampling of precipitation systems by the two methods over the prescribed period. Note that in spite of the rather limited temporal sampling by TMI and the rawinsondes, the 3-day mean surface rainfall rates are in fairly good agreement. The agreement between the TMI and rawinsonde analyses may be attributed, in part, to the large-scale forcing of precipitation during the observing period. For example, Johnson et al. (2004) noted that in the eleven-day period following monsoon onset (15-25 May), precipitation occurred nearly continuously within the range of the Bureau of Meteorology Research Centre C-POL radar located at Dongsha Island. Precipitation that is more strongly correlated in time tends to reduce the effects of intermittent sampling. Nevertheless, there are periods during which TMI rain rates are biased relative to the rawinsonde estimates.

For example, TMI estimates are high-biased in the 3-4 day periods centered on 15 and 24 May and 4 June, and are low biased on 6-7 June.

A time series of $Q_I - Q_R$ from TMI is shown in the second panel of Fig. 11. To make a more consistent comparison to the rawinsonde heating estimates, however, a rough correction for radiative heating/cooling is added to the TMI $Q_I - Q_R$ estimates to create the time series of TMI Q_I , shown in the third panel of Fig. 11. To make the correction, the net radiative heating/cooling profiles of Dopplack (1979) at 20°N latitude (March-May and June-August average; from his Figs. 6 and 7) are used to represent the mean radiative heating/cooling rate in the NESAs. The TMI Q_I estimate may be more directly compared to Q_I from the SCSMEX NESAs rawinsonde analyses shown in the fourth panel of Fig. 11.

First, note that the primary differences between the TMI and rawinsonde Q_I are correlated with differences in the estimates of surface rain rate. For example, the high bias of TMI Q_I on 15 and 24 May, and the low bias of Q_I on 7 June, are associated with similar biases in TMI surface rain rates at these times. Given that vertically-integrated latent heating is approximately equal to $L_v \cdot P$, it is not surprising that biases in heating and surface rain rate are correlated. These biases may be attributed to the low temporal resolution of the TMI estimates—on average the frequency of TMI observation of the NESAs was only $\sim 1.4 \text{ day}^{-1}$, while the sounding frequency was $\sim 3\text{-}4 \text{ day}^{-1}$.

In spite of differences in temporal sampling by the TMI and rawinsondes, the correspondence of the TMI and rawinsonde Q_I time series is reasonable. Heating maxima occur at about the same times and with similar magnitudes. Also, the transition from low-level heating starting 28 May to a single mid-level maximum on 4 June is captured by the TMI and rawinsondes. One notable difference in the time series occurs after 11 June, when upper level heating (altitudes greater than 12 km) is seen in the rawinsonde time series but not in the TMI series. Neither time series indicates significant precipitation during this period, and although the rawinsonde analysis suggests radiative heating of cirrus cloud, uncertainties in rawinsonde analyses are also greatest at high altitudes. Proper interpretation of the upper-tropospheric heating during this period will require greater scrutiny.

The mean TMI $Q_I - Q_R$, Q_I , and rawinsonde Q_I profiles for the 15 May – 20 June 1998 period are presented in Fig. 12. After correcting for the effects of radiative heating, the TMI heating profile shows reasonable consistency with the rawinsonde profile. The main

discrepancies are the excessive cooling in the TMI heating profile at the surface and below the melting level (~5 km). The cooling anomalies in the TMI profile could be explained by biases in the cloud-resolving model database: recent tests by S. Braun (personal communication) indicate high biases in the precipitation water contents produced by cloud resolving model simulations using standard bulk microphysics schemes. These biases would lead to a tendency for the V6 algorithm to select stratiform precipitation and heating vertical profiles over convective profiles from the algorithm's supporting database. A "stratiform bias" in estimated heating profiles would lead to stronger evaporative cooling at low levels and a deficiency of heating in the low-to mid-troposphere. Investigations are underway to identify the causes of high biases in precipitation water contents produced by current cloud-resolving model simulations.

5. Summary and Discussion

The objective of this study is to provide an initial evaluation of rain rate and latent heating estimates based upon an improved passive microwave radiometer algorithm (Version 6 or V6), applied to TRMM Microwave Imager (TMI) radiance observations over ocean backgrounds. The formulation of the algorithm and improvements, along with estimates of random errors, are described in Part I of the study. The V6 TMI estimates are compared to independent, collocated estimates from rain-gauge-calibrated radar at the Kwajalein Atoll ground validation site, as well as estimates from coincident spaceborne radar and a forerunning radiometer algorithm applied to TMI data (Version 5, or V5). Latent heating profiles from V6 TMI are compared to estimates based upon dual-Doppler observations at Kwajalein that are combined with thermodynamic profiles to obtain profiles of the vertical advection of dry static energy, a proxy for total diabatic heating. In addition, V6 TMI surface rain rate and latent heating time series are compared to time series derived from rawinsonde analyses of heat and moisture budgets over the Northern Enhanced Sounding Array of the South China Sea Monsoon Experiment.

In general, V6 TMI estimates of surface rain rate are consistent with estimates from ground-based or spaceborne radar, both in terms of instantaneous structure and quantitative precipitation amounts. The correlation of instantaneous, 0.5°-resolution V6 TMI estimates with respect to radar-based estimates does not change appreciably compared to V5; however, the high

bias previously noted in V5 estimates is significantly reduced. The overall reduced bias is attributed to the expanded cloud-resolving model database supporting the V6 algorithm, as well as the more consistent convective/non-convective rain separation procedure, which together reduce the previous high bias in estimated stratiform rains. The global reduction of bias in V6 TMI (relative to V5) estimates appears to hold regionally as well, but to varying degrees. High biases in monthly, 2.5°-resolution V6 TMI surface rain rate estimates are also reduced relative to V5. The minimization of bias in satellite rain estimates is critical for current data assimilation and climate analysis applications.

The convective contribution to rain rate is generally more difficult to estimate than total rain rate, owing to ambiguities in the separation of convective and stratiform rains based upon radiance spatial structures and polarization signatures in the TMI data. Even the evaluation of TMI algorithm estimates of convective rain rate is difficult, given differences in the way convective and stratiform rains are defined in the algorithm relative to ground-based or spaceborne radar observations. The apparent reduction of the stratiform high bias in the V6 TMI estimates, previously noted, suggests that the current convective/non-convective rain separation is superior to the separation method applied in V5. Independent confirmation of this result will require agreement on the definitions of convective and stratiform rain in TMI estimates and independent observations.

Although only limited comparisons of V6 TMI latent heating estimates to independent estimates are made in this study, the agreement between these estimates is reasonable, given the modest information content of the TMI data, differences in sampling between TMI and the independent measurement systems, and the general uncertainty in the independent estimates of heating. Comparisons of V6 TMI heating profiles to dual-Doppler profiles indicate that the altitude of maximum heating is tracked by the TMI estimates, although the detailed structure of the dual-Doppler profiles is not reproduced. The magnitude and altitude of the heating maximum in the mean SCSMEX NESAWinsonde-derived profile is also captured in the TMI-estimated profile. There are notable biases in the V6 TMI heating estimates, however, including excessive cooling near the surface and just below the freezing level. These biases are likely the result of biases in the precipitation water contents of cloud-resolving model simulations that support the V6 TMI algorithm.

The potential for improvement of the V6 passive microwave radiometer algorithm depends mainly on what can be done to reduce biases in the precipitation/latent heating estimates. Bringing additional information into the estimation problem is one approach for reducing biases, but much of the microwave radiance intensity and spatial structure information has already been exploited. Classification of storm type using the microwave observations and characterization of the storm environment from independent observations or model-based analyses could lead to more specific precipitation/latent heating estimates and reduced biases. Latent heating estimation should benefit most from storm type/environment information, since the heating distribution is strongly linked to storm kinematics.

Since V6 estimates are sensitive to the type and distribution of cloud-resolving model simulated profiles in the algorithm's supporting database, there is great potential for reducing algorithm biases by creating supporting databases that are more consistent with naturally-occurring profiles at the time/location where the algorithm is applied; see Shin and Kummerow (2003). A database constructed from hydrometeor profiles retrieved by applying a combined radar-radiometer algorithm to PR-TMI data is currently under development by the authors. This type of database has the advantage that each hydrometeor profile is unbiased with respect to both PR and TMI observations and is independent of cloud-resolving model assumptions (although some limited assumptions concerning vertical particle-size distributions are made). In addition, the natural distribution of profiles appropriate for a specific radiometer algorithm application can be derived by repeated application of the combined PR-TMI algorithm and sorting of the resulting profiles by storm type, storm environment, or other contextual conditions. Cloud model simulations would still be required to associate an appropriate vertical latent heating profile to each PR-TMI hydrometeor profile estimate.

The characterization of random errors in $0.5^\circ \times 0.5^\circ$ V6 TMI estimates using the error model developed in Part I appears to be consistent with the magnitudes of errors determined from comparisons of TMI and PR rain rate estimates. This model should be modified to account for errors in regions where the TMI algorithm identifies no rain, however. Another source of uncertainty is the potential error in simulated cloud-resolving model profiles that support the algorithm. If the algorithm's database is constructed from profiles derived from PR-TMI combined estimates, as previously discussed, then this error should be minimized. However, there will still be some uncertainty that a given profile in the database occurs with a prescribed

frequency, and this uncertainty can only be resolved by long-term statistical evaluation of how that profile frequency fluctuates for specified contextual conditions.

Sampling error appears to explain only a fraction of the total random error in monthly, 2.5°-resolution TMI estimates; the remaining error is attributed to physical inconsistency or non-representativeness of cloud-resolving model simulated profiles supporting the algorithm.

Overall, results of the evaluations of TMI surface rainfall rate and latent heating based upon independent measurements, along with results from Part I of this study, demonstrate that significant improvements have been made in V6 surface rain rate estimates relative to those from V5, and that rain rate and latent heating estimates from V6 have value for data assimilation and large-scale analysis applications.

Acknowledgments

TRMM datasets utilized in this study were accessed from the TRMM Science Data and Information System and the Goddard Space Flight Center Distributed Active Archive Center. David Wolff and David Marks of GSFC's Mesoscale Atmospheric Processes Branch provided analysis and helpful advice concerning Kwajalein ground validation radar estimates of rain rate. The University of Washington Mesoscale Group kindly supplied dual-Doppler radar datasets for selected cases. Estimates of Q_1 and surface rain rate based upon the SCSMEX rawinsonde network were provided by Paul Ciesielski and Richard Johnson of Colorado State University, whose expert advice is gratefully acknowledged. This research was supported by the NASA TRMM, Global Water and Energy Cycle, and Global Precipitation Measurement projects.

References

- Adler, R. F., G. J. Huffman, D. T. Bolvin, S. Curtis, and E. J. Nelkin, 2000: Tropical rainfall distributions determined using TRMM combined with other satellite and raingauge information. *J. Appl. Meteor.*, **39**, 2007-2023.
- Awaka, J., T. Iguchi, and K. Okamoto, 1998: Early results on rain type classification by the Tropical Rainfall Measuring Mission (TRMM) precipitation radar. *Proc. Eighth URSI Commission F Triennial Open Symp.*, Aveiro, Portugal, International Union of Radio Science, 143-146.
- Barrett, E.C., 1970: The estimations of monthly rainfall from satellite data. *Mon. Wea. Rev.*, **98**, 322-327.
- Barrett, E.C., and M.J. Beaumont, 1994: Satellite rainfall monitoring: An overview. *Remote Sensing Reviews*, **11**, 23-48.
- Cifelli, R., and S. A. Rutledge, 1998: Vertical motion, diabatic heating, and rainfall characteristics in North Australia convective systems. *Q. J. R. Meteor. Soc.*, **124**, 1133-1162.
- Davies-Jones, R. P., 1979: Dual-Doppler radar coverage area as a function of measurement accuracy and spatial resolution. *J. Appl. Meteor.*, **18**, 1229-1233.
- Doplick, T. G., 1979: Radiative heating of the global atmosphere. *J. Atmos. Sci.*, **36**, 1812-1817.
- Doviak, R. J., P. S. Ray, R. G. Strauch, and L. J. Miller, 1976: Error estimation in wind fields derived from dual-Doppler radar measurement. *J. Appl. Meteor.*, **15**, 868-878.
- Doviak, R.J., D.S., Zrnicek, 1993: Doppler radar and weather observations. 2nd edition, Academic press, 562 pp.
- Ebert, E.E., and M.J. Manton, 1998: Performance of satellite rainfall estimation algorithms during TOGA-COARE. *J. Atmos. Sci.*, **55**, 1537-1557.
- Haddad, Z.S., E.A. Smith, C.D. Kummerow, T. Iguchi, M.R. Farrar, S.L. Durden, M. Alves, and W.S. Olson, 1997: The TRMM 'Day-1' radar/radiometer combined rain-profile algorithm. *J. Meteor. Soc. Japan*, **75**, 799-809.
- Hollinger, J.P., J.L. Peirce, and G.A. Goe, 1990: SSM/I instrument evaluation. *IEEE Trans. Geosci. Rem. Sens.* **GE-28**, 781-790.
- Hou, A. Y., S. Q. Zhang, O. Reale, 2004: Variational continuous assimilation of TMI and SSM/I rain rates: Impact on GEOS-3 hurricane analyses and forecasts. *Mon. Wea. Rev.*, **132**, 2094-2109.

- Iguchi, T., T. Kozu, R. Meneghini, J. Awaka, and K. Okamoto, 2000: Rain-profiling algorithm for the TRMM precipitation radar. *J. Appl. Meteor.*, **39**, 2038-2052.
- Johnson, R. H., and P. E. Ciesielski, 2002: Characteristics of the 1998 summer monsoon onset over the northern South China Sea. *J. Meteor. Soc. Japan*, **80**, 561-578.
- Johnson, R. H., and P. E. Ciesielski, 2000: Rainfall and radiative heating rates from TOGA COARE atmospheric budgets. *J. Atmos. Sci.*, **57**, 1497-1514.
- Johnson, R. H., S. L. Alves, and P. E. Ciesielski, 2004: Organization of oceanic convection during the onset of the 1998 East Asian summer monsoon. *Mon. Wea. Rev.* (submitted).
- Kedem, B., L. Chiu, and G.R. North, 1990: Estimation of mean rain rate: Application to satellite observations. *J. Geophys. Res.*, **95**, 1965-1972.
- Kilonsky, B.J., and C.S. Ramage, 1976: A technique for estimating tropical open-ocean rainfall from satellite observations. *J. Appl. Meteor.*, **15**, 972-975.
- Krishnamurti, T. N., S. Surendran, D. W. Shin, R. J. Correa-Torres, T. S. V. V. Kumar, E. Williford, C. Kummerow, R. F. Adler, J. Simpson, R. Kakar, W. S. Olson, and F. J. Turk, 2001: Real-time multianalysis-multimodel superensemble forecasts of precipitation using TRMM and SSM/I products. *Mon. Wea. Rev.*, **129**, 2861-2883.
- Kummerow, C., Y. Hong, W.S. Olson, S. Yang, R.F. Adler, J. McCollum, R. Ferraro, G. Petty, D.-B. Shin, and T.T. Wilheit, 2001: The evolution of the Goddard profile algorithm (GPROF) for rainfall estimation from passive microwave sensors. *J. Appl. Meteor.*, **40**, 1801-1820.
- Lethbridge, M, 1967: Precipitation probability and satellite radiation data. *Mon. Wea. Rev.*, **95**, 487-490.
- Liao, L., R. Meneghini, and T. Iguchi, 2001: Comparisons of rain rate and reflectivity factor derived from the TRMM precipitation radar and the WSR-88D over the Melbourne, Florida, site. *J. Atmos. Oceanic Tech.*, **18**, 1959-1974.
- Mapes, B. E., P. E. Ciesielski, and R. H. Johnson, 2003: Sampling errors in rawinsonde-array budgets. *J. Atmos. Sci.*, **60**, 2697-2714.
- Mugnai, A., E.A. Smith, and G.J. Tripoli, 1993: Foundations for statistical-physical precipitation retrieval from passive microwave satellite measurements. Part II: Emission source and generalized weighting function properties of a time dependent cloud-radiation model. *J. Appl. Meteor.*, **32**, 17-39.
- Negri, A.J., and R.F. Adler, 1987a: Infrared and visible rain estimation. I: A grid cell approach. *J. Clim. Appl. Meteor.*, **26**, 1553-1564.

- Negri, A.J., and R.F. Adler, 1987b: Infrared and visible rain estimation. II: A cloud definition approach. *J. Clim. Appl. Meteor.*, **26**, 1565-1576.
- O'Brien, J. J., 1970: Alternative solutions to the classical vertical velocity problem. *J. Appl. Meteor.*, **9**, 197-203.
- Olson, W. S., C. D. Kummerow, Y. Hong, and W.-K. Tao, 1999: Atmospheric latent heating distributions in the Tropics derived from passive microwave radiometer measurements. *J. Appl. Meteor.*, **38**, 633-664.
- Olson, W. S., S. Yang, C. Kummerow, Z. Haddad, W.-K. Tao, Y. Wang, S. Lang, D. Johnson, S. Braun, C. Chiu, and J.-J. Wang, 2002: Estimation of precipitation and latent heating distributions from TRMM. *SPIE's Third International Asia-Pacific Environmental Remote Sensing Symposium*, Hangzhou, China, October 23-27.
- Palmen, E., and H. Riehl, 1957: Budget of angular momentum and energy in tropical cyclones. *J. Meteorol.*, **14**, 150-159.
- Schumacher, C., and R. A. Houze, Jr., 2000: Comparison of radar data from the TRMM satellite and Kwajalein oceanic validation site. *J. Appl. Meteor.*, **39**, 2151-2164.
- Shige, S., Y. N. Takayabu, W. K. Tao, and D. E. Johnson, 2004: Spectral Retrieval of Latent Heating Profiles from TRMM PR Data. Part I: Development of a Model-Based Algorithm. *J. Appl. Meteor.*, **43**, 1095-1113.
- Shin, D.-B. and C. Kummerow, 2003: Parametric rainfall retrieval algorithms for passive microwave radiometers. *J. Appl. Meteor.*, **42**, 1480-1496.
- Simpson, J., R.F. Adler, and G.R. North, 1988: A proposed satellite Tropical Rainfall Measuring Mission (TRMM). *Bull. Amer. Meteor. Soc.*, **69**, 278-295.
- Smith, E.A., A. Mugnai, H.J. Cooper, G.J. Tripoli, and X. Xiang, 1992: Foundations for statistical - physical precipitation retrieval from passive microwave satellite measurements. Part I: Brightness temperature properties of a time dependent cloud - radiation model. *J. Appl. Meteor.*, **31**, 506-531.
- Smith, E.A., X. Xiang, A. Mugnai, and G.J. Tripoli, 1994a: Design of an inversion-based precipitation profile retrieval algorithm using an explicit cloud model for initial guess microphysics. *Meteorol. Atmos. Phys.*, **54**, 53-78.
- Smith, E.A., C. Kummerow, and A. Mugnai, 1994b: The emergence of inversion-type precipitation profile algorithms for estimation of precipitation from satellite microwave measurements. *Remote Sensing Reviews*, **11**, 211-242.
- Smith, E.A., J. Lamm, R. Adler, J. Alishouse, K. Aonashi, E. Barrett, P. Bauer, W. Berg, A. Chang, R. Ferraro, J. Ferriday, S. Goodman, N. Grody, C. Kidd, D. Kniveton, C.

- Kummerow, G. Liu, F. Marzano, A. Mugnai, W. Olson, G. Petty, A. Shibata, R. Spencer, F. Wentz, T. Wilheit, and E. Zipser, 1998: Results of WetNet PIP-2 project. *J. Atmos. Sci.*, **55**, 1483-1536.
- Tao, W.-K., S. Lang, W. S. Olson, R. Meneghini, S. Yang, J. Simpson, C. Kummerow, E. Smith, and J. Halverson, 2001: Retrieved vertical profiles of latent heat release using TRMM rainfall products for February 1998. *J. Appl. Meteor.* **40**, 957-982.
- Weinman, J.A. and P.J. Guetter, 1977: Determination of rainfall distributions from microwave radiation measured by the Nimbus 6 ESMR. *J. Appl. Meteor.*, **16**, 437-442.
- Wilheit, T.T., A.T.C. Chang, M.S.V. Rao, E.B. Rodgers, and J.S. Theon, 1977: A satellite technique for quantitatively mapping rainfall rates over the oceans. *J. Appl. Meteor.*, **16**, 551-560.
- Wilheit, T., R. Adler, S. Avery, E. Barrett, P. Bauer, W. Berg, A. Chang, J. Ferriday, N. Grody, S. Goodman, C. Kidd, D. Kniveton, C. Kummerow, A. Mugnai, W. Olson, G. Petty, A. Shibata, E. Smith, and R. Spencer, 1994: Algorithms for the retrieval of rainfall from passive microwave measurements. *Remote Sensing Rev.*, **11**, 163-194.
- Wolff, D. B., D. A. Marks, E. Amitai, D. S. Silberstein, B. L. Fisher, A. Tokay, J. Wang, and J. L. Pippitt, 2004: Ground validation for the Tropical Rainfall Measuring Mission (TRMM). *J. Atmos. Oceanic Tech.* (submitted).
- Yamazaki, N., H. Kamahor, A. Yatagai, K. Takahashi, H. Ueda, K. Aonashi, K. Kuma, Y. Takeuchi, H. Tada, Y. Fukutomi, H. Igarashi, H. Fujinami, and Y. Kajikawa, 2000: On the release of GAME Reanalysis products, *Tenki*, **47**, 659-663 (in Japanese).
- Yang, S., and E.A. Smith: Moisture budget analysis of TOGA-COARE using SSM/I retrieved latent heating and large scale Q_2 estimates, 1999a. *J. Atmos. Oceanic Technol.*, **16**, 633-655.
- Yang, S., and E.A. Smith, 1999b: Four dimensional structure of monthly latent heating derived from SSM/I satellite measurements. *J. Climate*, **12**, 1016-1037.
- Yang, S., and E. A. Smith, 2000: Vertical Structure and transient behavior of convective-stratiform heating in TOGA COARE from combined satellite-sounding analysis. *J. Appl. Meteor.*, **39**, 1491-1513.
- Yang, S., and E.A. Smith, 2004: Mechanisms for diurnal variability of global tropical rainfall observed from TRMM. *J. Climate* (submitted).

Tables:

Table 1. Comparison of instantaneous, $0.5^\circ \times 0.5^\circ$ precipitation products over ocean at the Kwajalein GV site during 1998. V6 and V5 are the statistics of the TMI surface rain rate estimates from the Version 6 and Version 5 algorithms, respectively. CONV are the statistics of the V6 TMI estimates of convective rain rate.

Statistic	TMI vs. GV			TMI vs. PR		
	V6	V5	CONV	V6	V5	CONV
Sample	62	62	54	72	72	54
TMI Mean	0.67	0.65	0.60	0.29	0.32	0.29
Ratio	0.70	0.68	0.85	1.03	1.13	1.60
Err. Std.	0.71	0.78	0.73	0.30	0.32	0.36
Correl.	0.83	0.80	0.75	0.84	0.79	0.72

Table 2. Comparison of instantaneous, $0.5^\circ \times 0.5^\circ$ precipitation products over ocean during July 2000. V6 and V5 are the statistics of the TMI surface rain rate estimates from the V6 and V5 algorithms, respectively. CONV are the statistics of the V6 TMI estimates of convective rain rate.

TMI vs. PR			
Statistic	V6	V5	CONV
Sample	258558	258558	119201
TMI Mean	0.26	0.28	0.33
Ratio	0.98	1.08	1.26
Err. Std.	0.44	0.50	0.58
Correl.	0.88	0.89	0.75

Table 3. Boundaries of $10^\circ \times 10^\circ$ domains selected for regional analyses presented in Figs. 7 and 8.

Region	Latitude / Longitude Domain
West Pacific (WP)	$5^\circ\text{S} - 5^\circ\text{N} / 150^\circ\text{E} - 160^\circ\text{E}$
East Pacific (EP)	$0^\circ - 10^\circ\text{N} / 105^\circ\text{W} - 95^\circ\text{W}$
Atlantic Ocean (AO)	$0^\circ - 10^\circ\text{N} / 40^\circ\text{W} - 30^\circ\text{W}$
Indian Ocean (IO)	$5^\circ\text{S} - 5^\circ\text{N} / 80^\circ\text{E} - 90^\circ\text{E}$
South China Sea (SCS)	$10^\circ\text{N} - 20^\circ\text{N} / 110^\circ\text{E} - 120^\circ\text{E}$

Figure Captions:

Fig. 1. Map of the Kwajalein Atoll and vicinity, showing the locations of radars on Kwajalein and the Research Vessel Ron H. Brown, the domain of rain observations provided the Kwajalein radar, and the dual-Doppler coverage provided by the two radars. This was the configuration of radars during the KWAJEX field campaign.

Fig. 2. The sequence of all rain events in 1998 observed coincidentally by ground validation radar at Kwajalein, and by TMI and PR on the TRMM satellite. The ground validation rain maps shown are identified by the radar volume scan date (yyymmdd) and time (hhmmss). Distances are relative to the radar location in kilometers.

Fig. 3. Map of the northern South China Sea, showing the polygonal domain of the Northern Enhanced Sounding Array (NESA). Rawinsonde launch sites are located at the vertices of the polygon and on Dongsha Island and the Research Vessel Shiyan #3 in the interior of the polygon. The NESA was a domain of intensive observations during SCSMEX.

Fig. 4. Comparisons of instantaneous surface rain rates (over ocean) near Kwajalein Atoll from matched GV radar, PR, and TMI at TMI product resolution (14 km x 14 km). In the left column are surface rain rate estimates from V6 TMI, the Kwajalein radar, and V5 TMI at approximately 17 UTC on 24 August 1998. In the right column are rain rate estimates from V6 TMI, PR, and V5 TMI at approximately 17 UTC on 28 October 1998.

Fig. 5. Scatterplots of instantaneous, $0.5^\circ \times 0.5^\circ$ average (a) total surface rain rates and (b) convective rain rates from V6 TMI (top panels) and V5 TMI (bottom panels) versus Kwajalein radar and PR, based upon 21 selected TRMM overpasses of Kwajalein in 1998.

Fig. 6. (a) Scatterplots of instantaneous, $0.5^\circ \times 0.5^\circ$ average total surface rain rates (top panels) and convective rain rates (bottom panels) from V6 TMI (left column) and V5 TMI (right column) versus PR. (b) Scatterplots of instantaneous, $0.5^\circ \times 0.5^\circ$ average total surface rain rates for which the PR convective fraction is greater than 50% (top panels) and less than 50% (bottom panels) from V6 TMI (left column) and V5 TMI (right column) versus PR. Plots are based upon all collocated observations over ocean from July 2000. Overlaid on the V6 TMI plot of total surface rain rates in (a) are bounds of the estimated mean error (dashed lines; see text for description).

Fig. 7. Scatterplots of instantaneous, $0.5^\circ \times 0.5^\circ$ average surface rain rates from V6 TMI (left column) and V5 TMI (right column) versus for five selected $10^\circ \times 10^\circ$ tropical domains over the Western Pacific Ocean, Eastern Pacific Ocean, Atlantic Ocean, Indian Ocean, and South China Sea, respectively. The tropical domains are defined in Table 3.

Fig. 8. Bivariate statistics for the intercomparison of instantaneous, $0.5^\circ \times 0.5^\circ$ average surface rain rates from V6 TMI (left panel) and V5 TMI (right panel) versus PR for the five selected tropical oceanic domains defined in Table 3. Abscissa indices 1, 2, 3, 4, and 5 correspond to the Western Pacific Ocean, Eastern Pacific Ocean, Atlantic Ocean, Indian Ocean, and South China Sea, respectively. Plotted are the TMI/PR bias ratio (solid line), correlation coefficient (dashed line), and error standard deviation (dotted line).

Fig. 9. Plots of monthly, $2.5^\circ \times 2.5^\circ$ resolution V6 TMI (left panel) and V5 TMI (right panel) rain rate estimates versus PR estimates, based upon collocated TMI and PR observations over ocean from July 2000. Superimposed on the V6 TMI rain rates are bounds of the estimated mean sampling error of TMI (dashed lines, see text for description).

Fig. 10. Comparisons of V6 TMI and dual-Doppler-radar study (DDS) heating profiles for two selected TRMM overpasses of Kwajalein Atoll. Shown in the left column are plan views of surface rain rates from the Doppler radar measurements. In the right column are vertical profiles of Q_I-Q_R from V6 TMI (solid line), overlaid on plots of estimated Q_I from DDS (various dashed lines) for different assumed bias errors, ranging from 0 – 30%. Data shown in (a) correspond to the TRMM overpass at approximately 10 UTC on 15 August 1999, while those in (b) correspond to the overpass at 19 UTC on 29 July 1999.

Fig. 11. Time series of NESAs-averaged surface rain rate, V6 TMI Q_I-Q_R , V6 TMI Q_I , and rawinsonde analysis of Q_I over the period 15 May – 20 June, 1998, during SCSMEX. Surface rain rates are derived from both V6 TMI and the rawinsonde Q_2 budget. A 3-day running mean filter is applied to all data in the time series. Heating profile time series are contoured at $-1, 0, 1, 2, 4,$ and $8 \text{ }^\circ\text{K day}^{-1}$.

Fig. 12. Mean V6 TMI Q_I-Q_R (solid line), V6 TMI Q_I (dashed line), and rawinsonde analysis Q_I (dotted line) profiles for the period 15 May – 20 June, 1998, over the SCSMEX NESAs.

KWAJEX Radar Domains

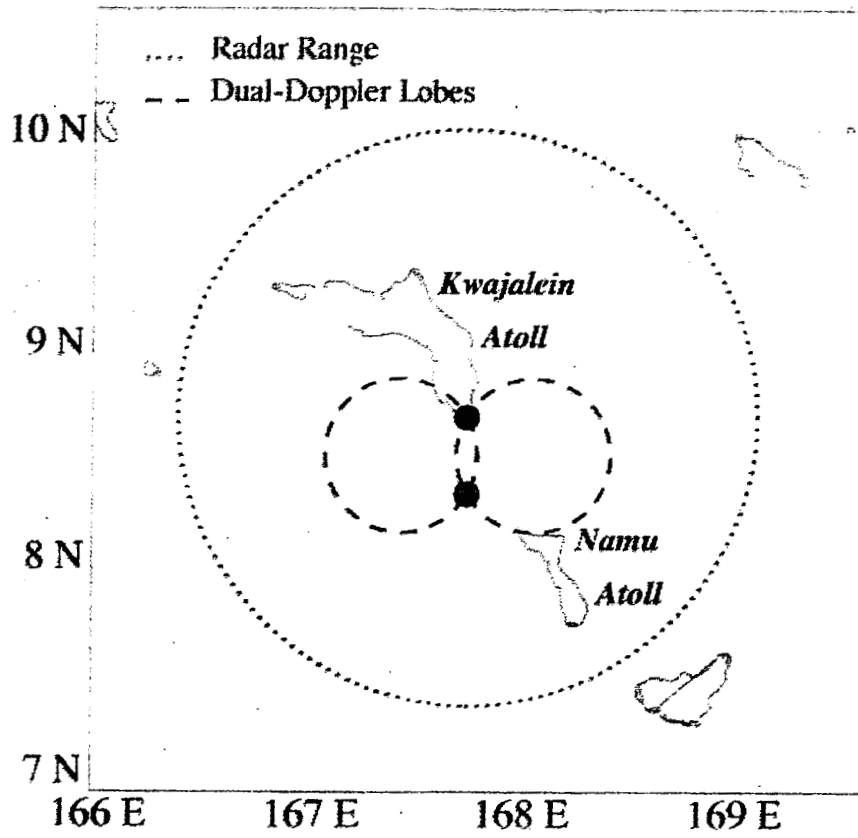


Fig. 1

Surface Rain Rate from the Kwajalein Radar

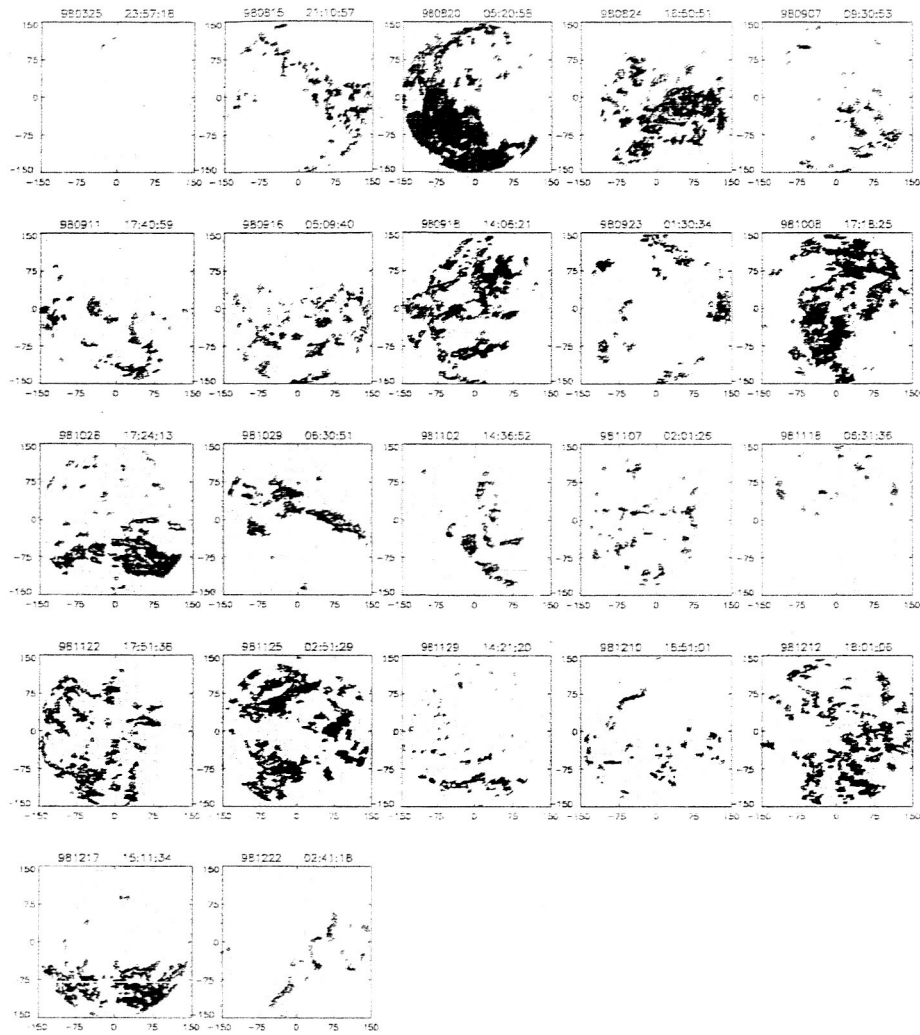


Fig. 2

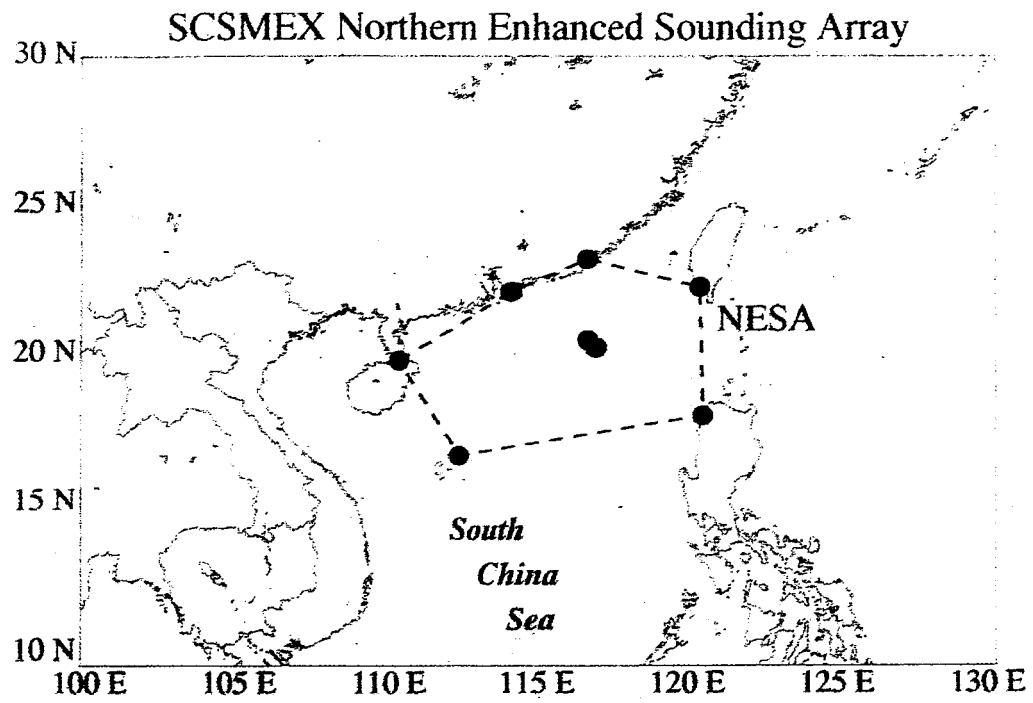


Fig. 3

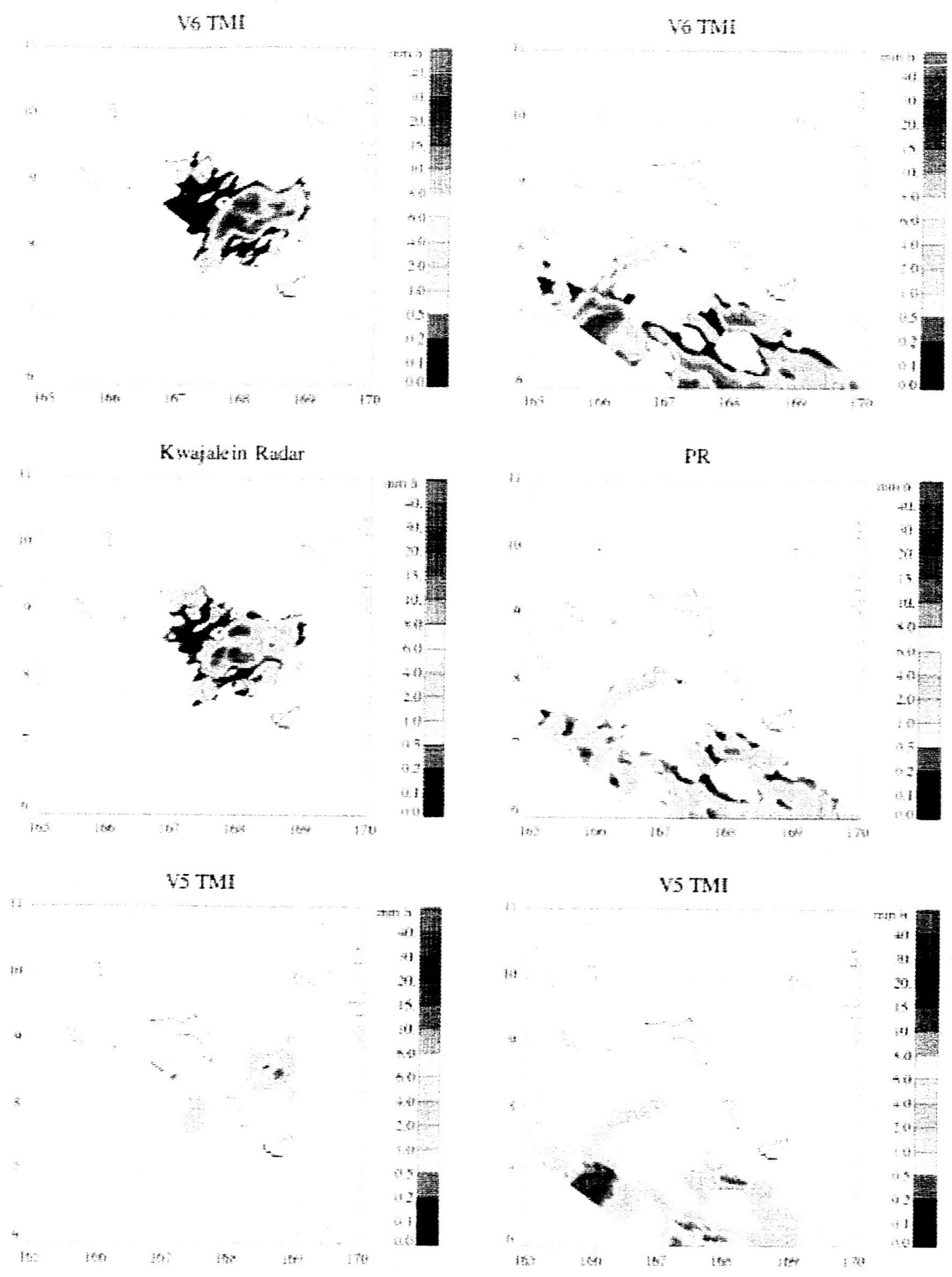


Fig. 4

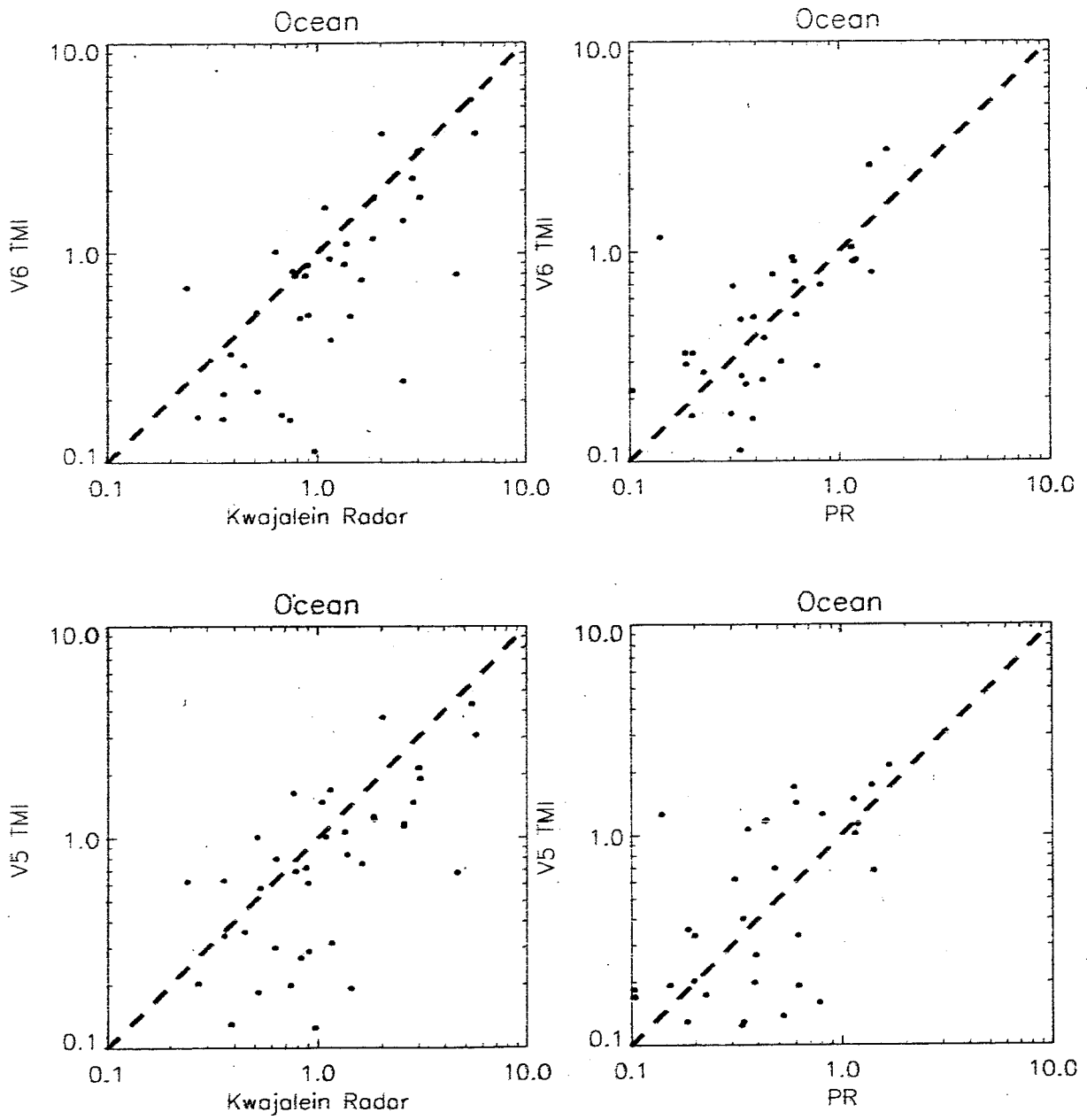


Fig. 5a

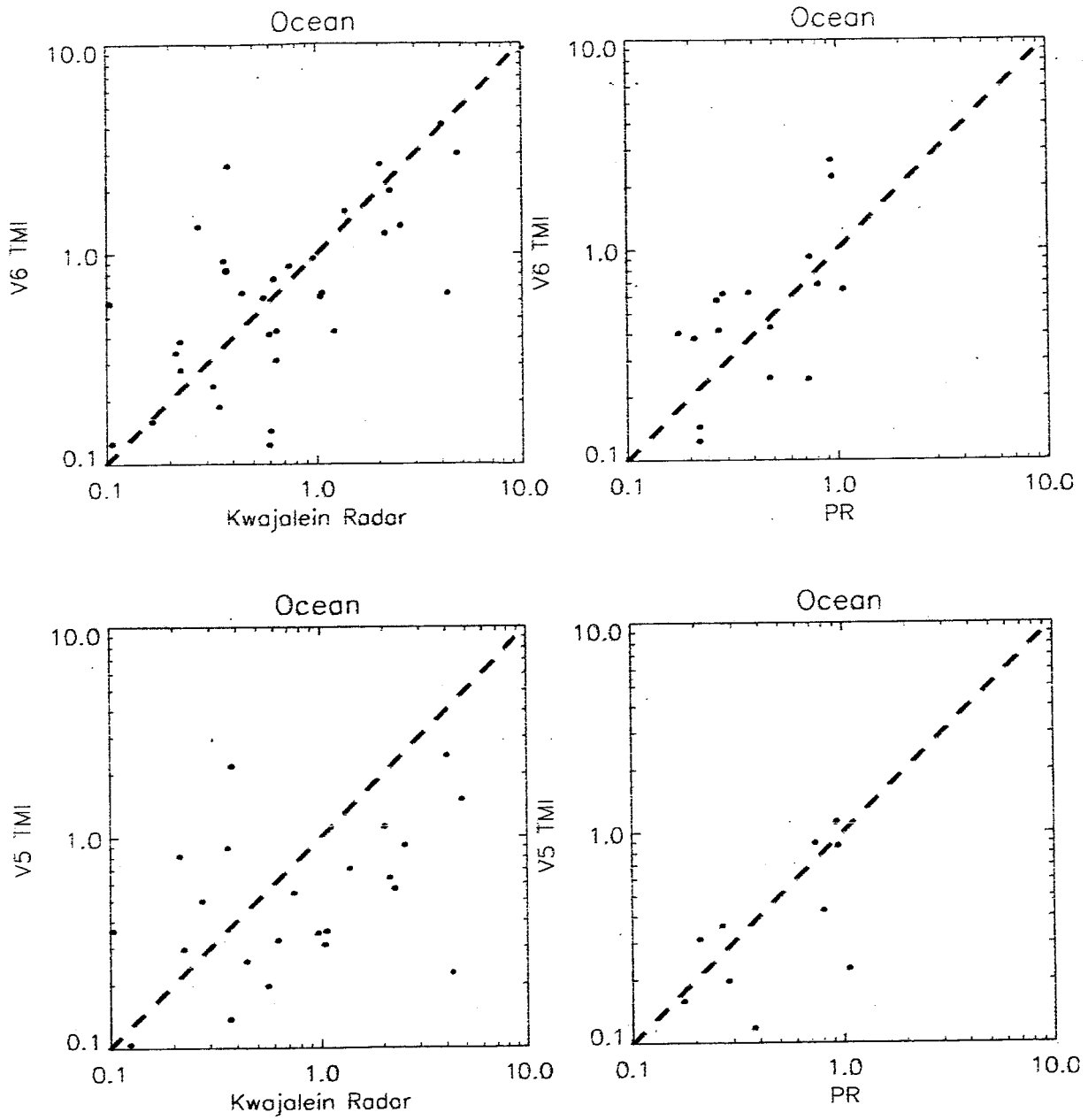


Fig. 5b

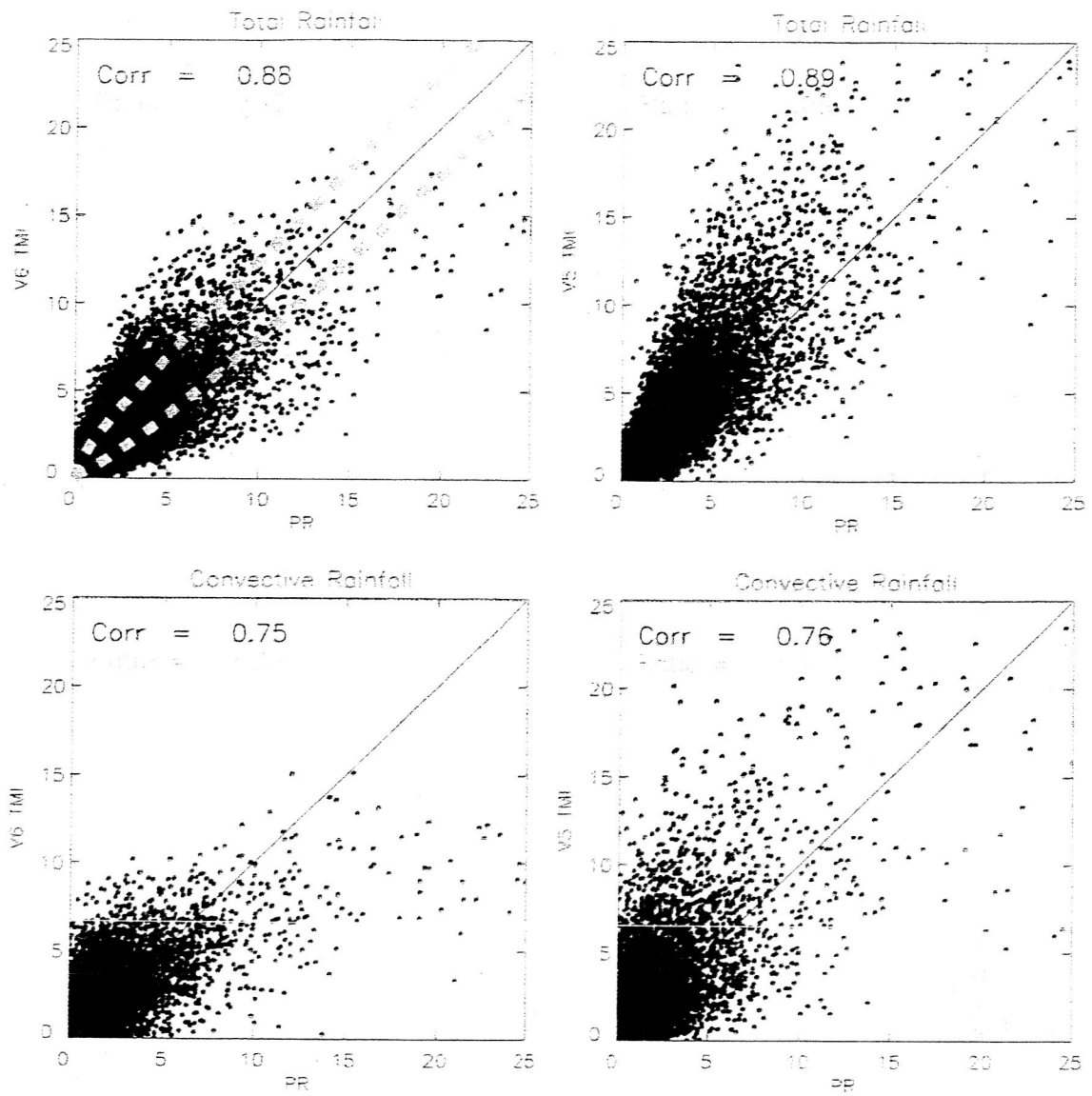


Fig. 6a

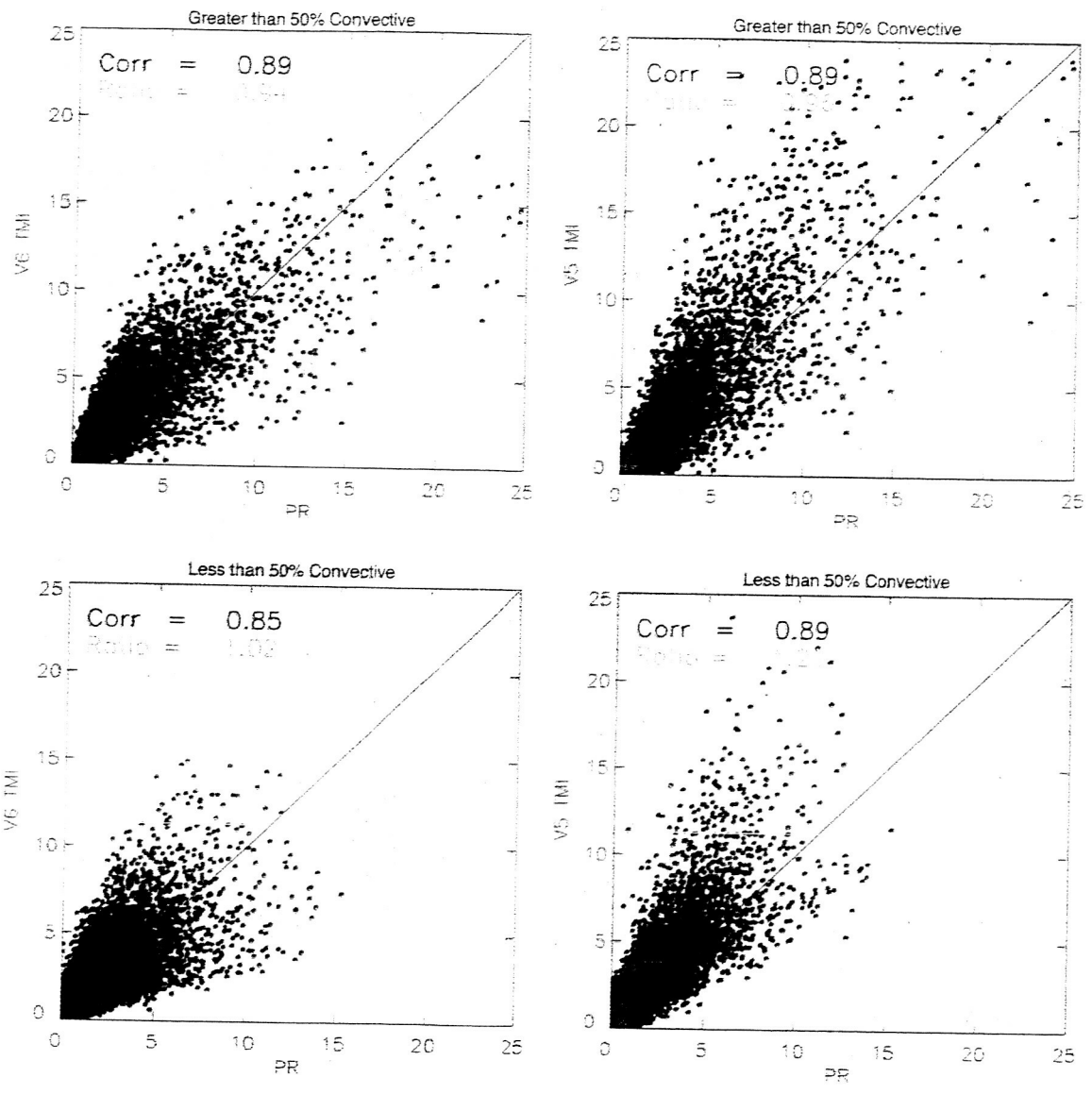


Fig. 6b

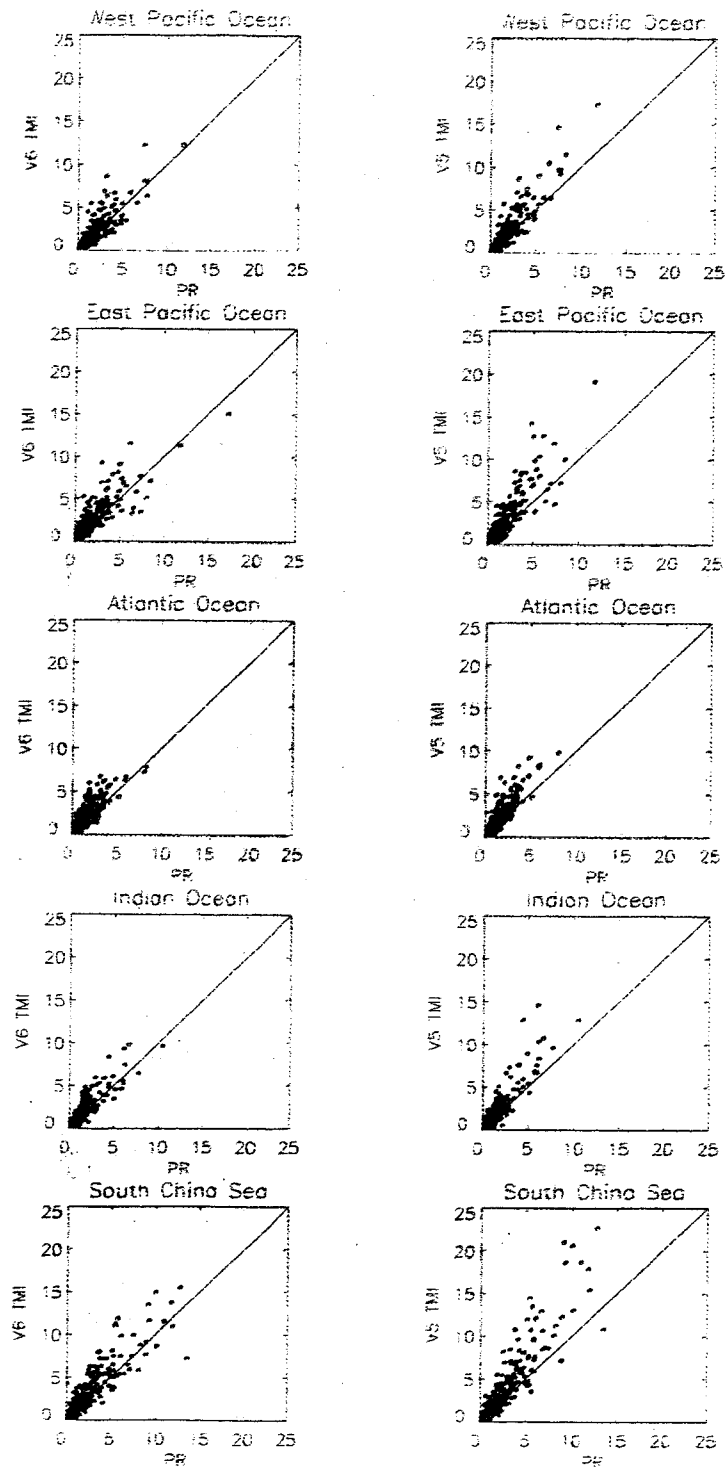


Fig. 7

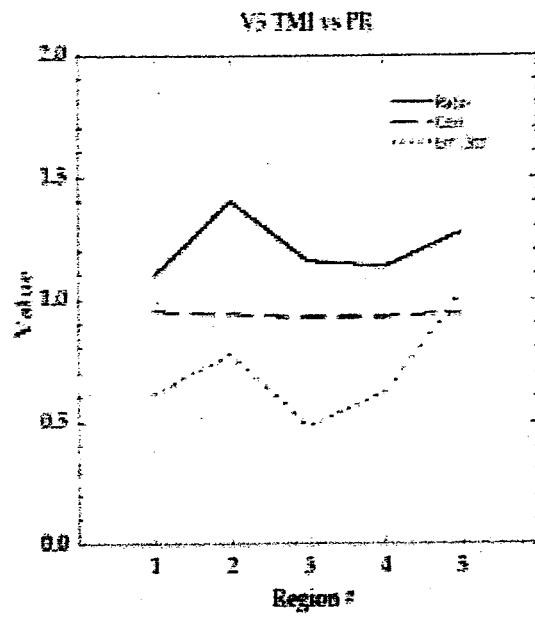
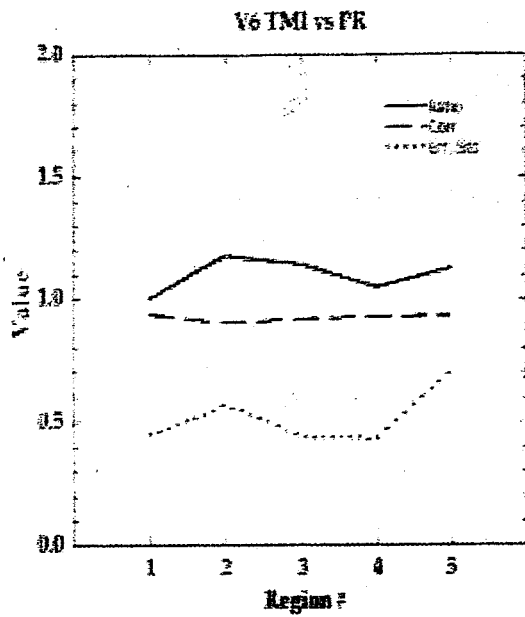


Fig. 8

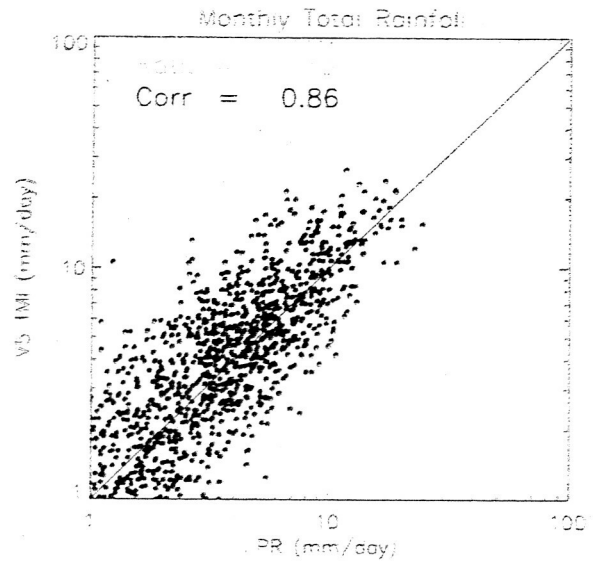
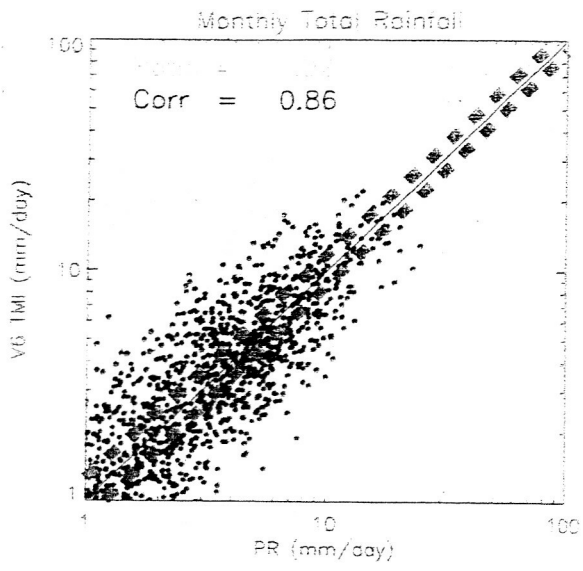


Fig. 9

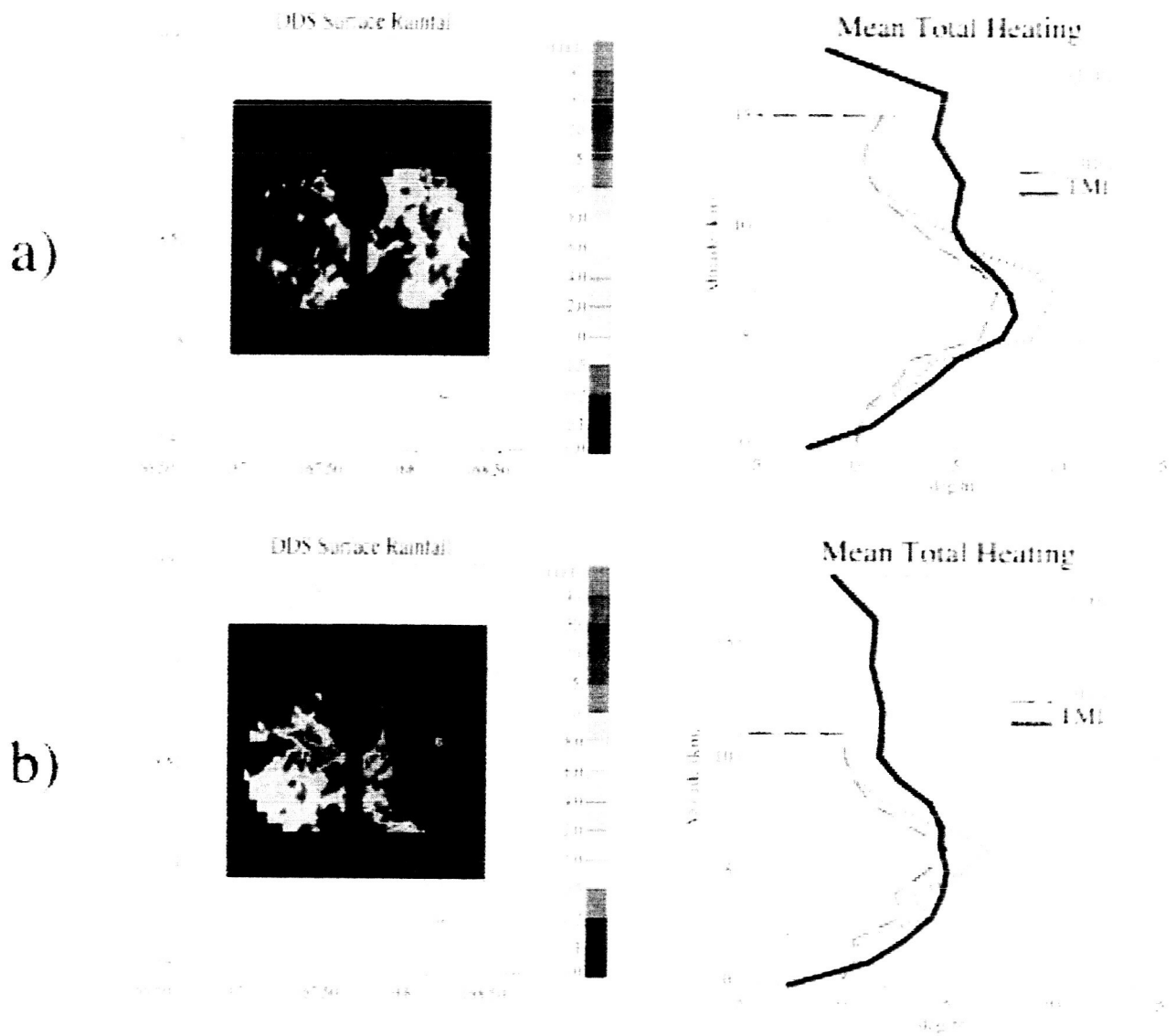


Fig. 10

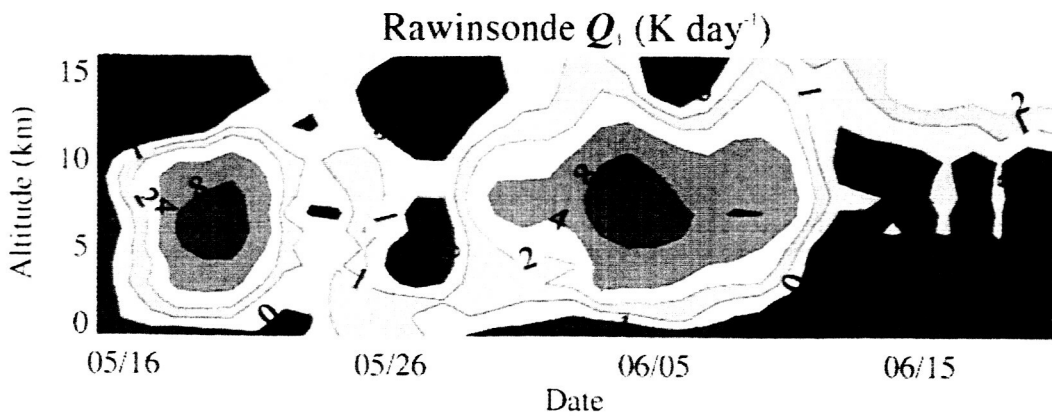
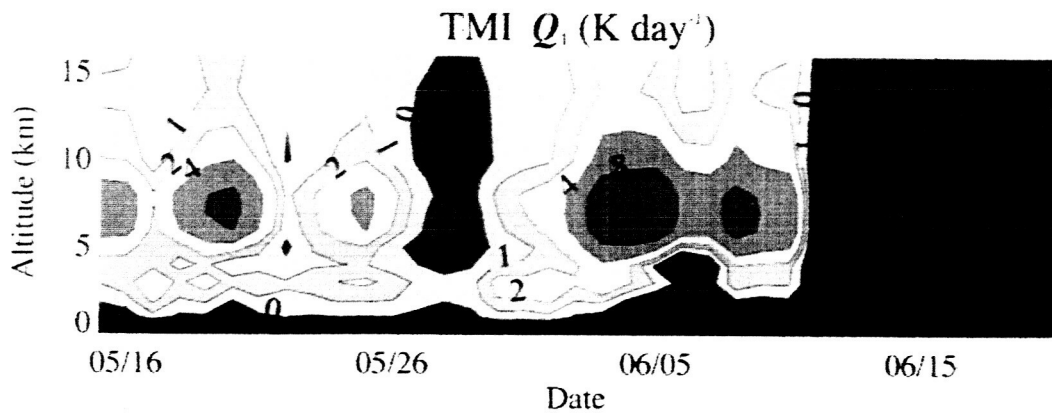
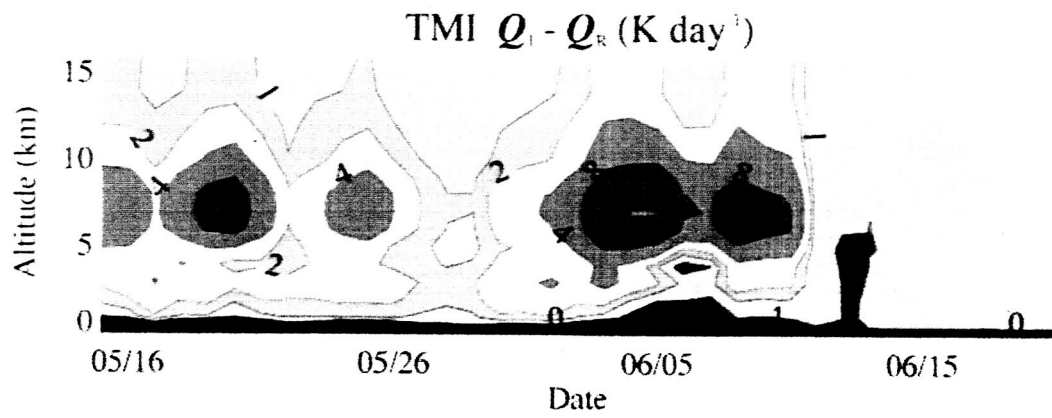
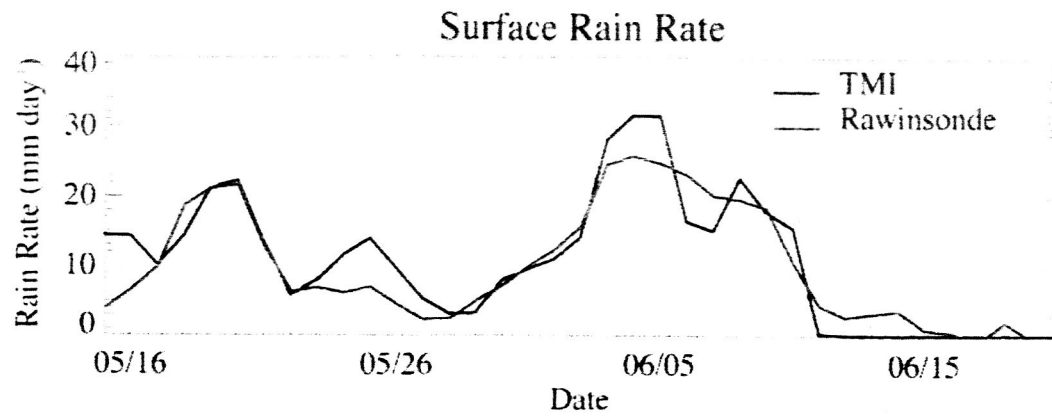


Fig. 11

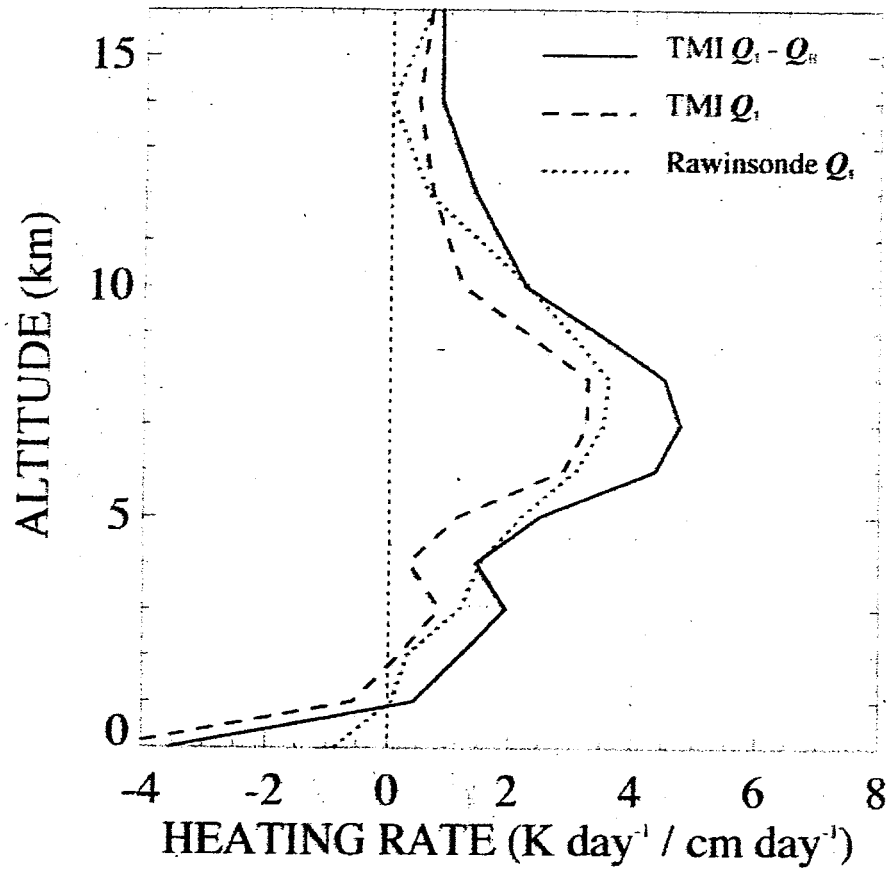


Fig. 12

10/15/04

Popular Summary

Precipitation and Latent Heating Distributions from Satellite Passive Microwave Radiometry

Part I: Method and Uncertainties, and

Part II: Evaluation of Estimates Using Independent Data

A basic process in clouds is the transformation of water in the vapor phase to the liquid or solid phase. This process produces not only precipitation (rain or snow) but also latent heat, which is released into the atmosphere as the water molecules go from the higher to the lower energy states. A knowledge of the distributions of precipitation over the globe is essential for studying the earth's climate and the cycling of water through the earth-atmosphere system. The distributions of latent heating tell us how variations in buoyancy drive circulations in the atmosphere and how the sun's energy (which is consumed in the evaporation of surface moisture) is redistributed by the atmosphere to regions of more intense precipitation (and thus more intense latent heating).

In Part I of this study, an improved method for estimating precipitation and latent heating distributions from satellite-borne passive microwave radiometer measurements is described. A key feature of this method are the improved models of clouds and precipitation that are used to create a kind of reference "library" of possible solutions that the method can draw upon. If simulated microwave radiances associated with a particular cloud/precipitation model in the library are consistent with radiances actually observed by the satellite microwave radiometer, then it is assumed that that particular model is a likely solution. The models of cloud and precipitation are not perfect, however: errors in the models can result in errors in inferred precipitation or latent heating from the estimation method. In the current study, the physics of precipitating ice particles in the models is improved to remove a significant source of error in the modeled clouds. Another important advance is the way convective and stratiform precipitation areas are separated by the estimation method. Convective regions are associated with intense rainfall and strong upward and downward air motions in the precipitating clouds, while stratiform rain is gentle and widespread, and the associated air motions are relatively weak. By initially classifying a given region as convective or stratiform based upon the microwave radiometer observations, a more specific precipitation or latent heating estimate can be made. An improved technique for separating convective and stratiform regions using the horizontal variation of observed microwaves and their polarization is employed in the revised estimation method.

The improved method is scrutinized to determine what levels of error can be expected in estimated precipitation and latent heating. If rain rate estimates are averaged over $0.5^\circ \times 0.5^\circ$ boxes, their errors are expected to be about 50% for a 1 mm per hour rain rate but decrease to 20% at 14 mm per hour. If the rain rate estimates are accumulated in $2.5^\circ \times 2.5^\circ$ boxes and then averaged over 1 month, the anticipated errors in the resulting monthly rain rates can be up to 35% for moderate rain rates. The primary source of error in the monthly-average rain estimates is the limited sampling, about 1 per day, by the